PHYSICAL REVIEW D

PARTICLES AND FIELDS

THIRD SERIES, VOL. 1, NO. 7 1 APRIL 1970

Neutron-Proton Elastic Scattering from 2 to 7 GeV/c†

M. L. PERL AND J. COX
Stanford Linear Accelerator Center, Stanford University, Stanford, California 94305

AND

MICHAEL J. LONGO
Randall Laboratory of Physics, University of Michigan, Ann Arbor, Michigan 48104

AND

M. N. KREISLER
Palmer Physical Laboratory, Princeton University, Princeton, New Jersey 08540

(Received 9 October 1969)

Direct measurements were made of neutron-proton elastic scattering differential cross sections at high energies. A neutron beam with a continuous momentum spectrum between 1.2 and 6.7 GeV/c was scattered off a liquid hydrogen target, and spark chambers were used to determine the neutron scattering angle and, in a proton spectrometer, to measure the momentum and scattering angle of the recoil proton. Differential cross sections are presented over the incident neutron momentum range in intervals of the order of 0.5-GeV/c wide. The cross sections have an exponential peak in the forward direction and then flatten and become isotropic about the 90° c.m. scattering angle. At larger angles, the cross sections again rise towards the expected charge-exchange peak, which was not within the range of this experiment. There is little evidence of any other structure in the cross section. Values are presented for the slope of the diffraction peak, and comparisons are made between these slopes, and the 90° c.m. cross sections, for pp and np elastic scattering. The results presented here differ from those previously reported because of an error in a Monte Carlo calculation and in the availability of improved data on the real part of the np elastic scattering amplitude. At 5 GeV/c, a direct comparison of pp and np data allows the $I=0$ differential cross section to be extracted. The np data have been fitted in powers of $\cos\theta_{\text{c.m.}}$ for $|\cos\theta_{\text{c.m.}}|<0.8$ for each energy range.

I. INTRODUCTION

THE elastic scattering of neutrons from protons was studied at incident neutron laboratory momenta between 2 and 7 GeV/c in an optical spark-chamber experiment with the object of extending the range of measurements of the differential cross sections for this interaction to higher energies than had been previously examined.[1-4] The np system has been measured in great detail for momenta at or below 1.3 GeV/c.[5] There are only a handful of experiments between 1.3 and 1.7 GeV/c, some of which cover only small angular regions in the c.m. system.[6-8] Above 1.7 GeV/c, the only previous measurements which had been made were in the angular region near 180° (i.e., the charge-exchange region).[9,10] The lack of experiments at high energies was largely due to the difficulty of obtaining monochromatic neutron beams, the presence of large inelastic backgrounds, and the problem of constructing efficient, reliable high-energy neutron

---

† Work supported in part by the U. S. Office of Naval Research under Contract No. NONR 1224(23) and the U. S. Atomic Energy Commission.

[1] M. N. Kreisler, F. Martin, M. L. Perl, M. J. Longo, and S. T. Powell, III, Phys. Rev. Letters **16**, 1217 (1966).

[2] M. N. Kreisler, Stanford Linear Accelerator Report No. SLAC-66, 1966 (unpublished).

[3] J. Cox, M. L. Perl, M. N. Kreisler, M. J. Longo, and S. T. Powell, III, Phys. Rev. Letters **21**, 641 (1968).

[4] J. Cox, M. L. Perl, M. N. Kreisler, and M. J. Longo, Phys. Rev. Letters **21**, 645 (1968).

[5] R. Wilson, *The Nucleon-Nucleon Interaction, Experimental and Phenomenological Aspects* (Wiley-Interscience, Inc., New York, 1963).

[6] N. S. Amaglobeli and Yu. M. Kazarinov, Zh. Eksperim. i Teor. Fiz. **33**, 53 (1958); **37**, 1587 (1959) [English transls.: Soviet Phys. JETP **7**, 37 (1958); **10**, 1125 (1960)].

[7] G. Martelli, H. B. van der Raay, R. Rubinstein, K. R. Chapman, J. D. Dowell, W. R. Frisken, B. Musgrave, and D. H. Reading, Nuovo Cimento **21**, 581 (1961).

[8] R. R. Larsen, Nuovo Cimento **18**, 1039 (1960); Lawrence Radiation Laboratory, UCRL Report No. 9292, 1962 (unpublished).

[9] H. Palevsky, J. A. Moore, R. L. Stearns, H. R. Muether, R. J. Sutter, R. E. Chrien, A. P. Jain, and K. Otnes, Phys. Rev. Letters **9**, 509 (1962); J. L. Friedes, H. Palevsky, R. L. Stearns, and R. J. Sutter, *ibid.* **15**, 38 (1965).

[10] G. Manning, A. G. Parham, J. D. Jafar, H. B. van der Raay, D. H. Reading, D. G. Ryan, B. D. Jones, J. Malos, and N. H. Lipman, Nuovo Cimento **41A**, 167 (1966).

detectors. After this experiment was carried out and the initial results were analyzed,[1,2] proving the method, two higher-energy experiments were performed using the same method.[11,12]

There are two reasons for the interest in measuring neutron-proton elastic scattering at high energies. First, it is the only nucleon-nucleon system which allows the investigation of scattering angles greater than 90° in the c.m. system; in the proton-proton system the particle symmetry allows measurements only from 0 to 90°. The second reason is that the neutron-proton and proton-proton systems are related through the concept of isotopic spin. At low energies this restricts the relative behavior of the proton-proton and neutron-proton systems, but the elastic scattering of the two systems can still differ. At very high energies, it has generally been assumed that the isotopic spin differences between the neutron-proton and proton-proton systems will not cause large differences in their behavior. For example, it is usually assumed that at very high energies the neutron-proton and proton-proton total cross sections will become equal. Similarly, it is usually assumed that at very high energies the small-angle elastic scattering of the neutron-proton and proton-proton systems will become equal. But regardless of the energy, for elastic scattering at greater than 90° in the barycentric system, the symmetry considerations previously mentioned prevent neutron-proton and proton-proton elastic scattering from being equal. Therefore, comparison of elastic scattering of neutron-proton and proton-proton systems at high energies and over a large angular region extending past 90° in the barycentric system involves basic consideration of the influence of isotopic spin at very high energies and touches on basic quantum-mechanical principles of symmetry.

For the reasons given in the previous paragraph it seemed to us to be very important to make detailed measurements of neutron-proton elastic scattering at reasonably high energies. We decided to carry out the first experiment in the momentum range 2–7 GeV/*c* with a neutron beam produced by the external proton beam of the Bevatron. A unique experimental method was devised for measuring neutron-proton elastic scattering simultaneously over a large range of energies. This method is described briefly in the next paragraph and in more detail in Sec. III. We have since extended this method to much higher momenta, namely, 28.5 GeV/*c*, using the internal beam of the alternating gradient synchrotron (AGS) of the Brookhaven National Laboratory, and that experiment is now being analyzed.[11] In this paper we limit ourselves to summarizing the results of the Bevatron experiment, results which have been given in brief form in previous publications.

In the present experiment a neutron beam with a broad spectrum of incident momenta was used with a liquid-hydrogen target. The exit angle and momentum of the positively charged recoil particle and the exit angle of the scattered neutral particle were found using optical spark chambers. When the incoming particle was assumed to be a neutron and the outgoing particles a neutron and proton, this information overdetermined the event and allowed a two-constraint fit to be made. Cuts were made on the raw data to exclude events which gave a bad fit to the elastic kinematics. Apart from a small number of true elastic scattering events which had bad fits, these events were due to inelastic neutron-proton scattering and scattering of beam contaminants. The rejected events were used to estimate the background contamination in the accepted events, and a suitable subtraction (usually small) was made to obtain the final cross sections.

II. THEORY

In this paper we are concerned only with comparing the behavior of neutron-proton elastic scattering with other hadron-hadron elastic scattering phenomena. In particular, we are interested in comparing neutron-proton and proton-proton elastic scattering with reference to the relationships of the two isotopic spin states. Therefore, we shall omit any general theoretical discussion of elastic scattering from any of the basic points of view, such as that of the optical model or of Regge theory; but where necessary, we shall refer to the more empirical concepts derived from the Regge theory.

The analysis of the nucleon-nucleon system is plagued by the large number of scattering amplitudes. If one considers first the case of the two completely different spin-$\frac{1}{2}$ particles, *a* and *b*, then using helicity amplitudes it is easy to count the number of independent elastic scattering amplitudes. We denote the four-momentum and helicity states of the particles as follows:

	Four-momentum	Helicity
Incident particle *a*	$p_a=(E_a,\mathbf{p}_a)$	λ_a
Incident particle *b*	$p_b=(E_b,\mathbf{p}_b)$	λ_b
Final particle *a*	$p_a'=(E_a',\mathbf{p}_a')$	λ_a'
Final particle *b*	$p_b'=(E_b',\mathbf{p}_b')$	λ_b'

The square of the total energy in the barycentric system is the invariant s, where $s=(p_a+p_b)^2$. Finally, θ is the barycentric angle between $\mathbf{p}_a$ and $\mathbf{p}_a'$. A particular helicity amplitude will be denoted by $F_{\lambda_a'\lambda_b',\lambda_a\lambda_b}(\theta)$ and is a function of (s,θ), although the s is not always written explicitly. Furthermore, we shall use the subscripts $+$ and $-$ to denote $\lambda_a=+\frac{1}{2}$ and $-\frac{1}{2}$, respectively, and similarly for λ_b, λ_a', and λ_b'.

In this theory section and in the entire paper, unless otherwise stated, all angles and all differential cross sections $(d\sigma/d\Omega)$ are in the barycentric system. The

---

[11] M. J. Longo, in CERN Report No. 68-7, 1968, p. 523 (unpublished).

[12] J. Engler, K. Horn, J. Konig, F. Monnig, P. Schludecker, H. Schopper, P. Sievers, H. Ullrichand, and K. Runge, Phys. Letters **29B**, 321 (1969).

energy or momentum of the incident neutron, unless otherwise stated, is in the laboratory system.

The normalization of $F_{\lambda_a'\lambda_b',\lambda_a\lambda_b}(\theta)$ is defined by

$$(d\sigma/d\Omega)_{\lambda_a'\lambda_b',\lambda_a\lambda_b}=|F_{\lambda_a'\lambda_b',\lambda_a\lambda_b}(\theta)|^2, \tag{1}$$

where $(d\sigma/d\Omega)$ is the differential cross section in the barycentric system for the helicity states $|\lambda_a,\lambda_b\rangle\rightarrow|\lambda_a',\lambda_b'\rangle$ and has the unit mb/sr.

The 16 possible helicity amplitudes[13] are reduced to eight by parity conservation and then to six by time reversal invariance. These six amplitudes are

$$F_{++,++}(\theta),\ F_{+-,++}(\theta),\ F_{-+,++}(\theta),\ F_{--,++}(\theta),$$
$$F_{+-,+-}(\theta),\ \text{and}\ F_{-+,+-}(\theta).$$

Next consider the case of two identical nucleons, namely, the pp system. Here again, there would be six helicity amplitudes; however, the identity of the two protons further reduces the number of amplitudes and also requires symmetry relations about $\theta=\pi/2$. For example, $F_{--,++}(\theta)$ must be equal to $\pm F_{--,++}(\pi-\theta)$ because there is no way to distinguish the two cases by observation. The symmetry relations about $\theta=\pi/2$ are for the pp case as follows (the superscript pp denotes the pp amplitudes):

$$\begin{aligned}
F_{++,++}{}^{pp}(\pi-\theta)&=+F_{++,++}{}^{pp}(\theta),\\
F_{--,++}{}^{pp}(\pi-\theta)&=+F_{--,++}{}^{pp}(\theta),\\
F_{+-,++}{}^{pp}(\pi-\theta)&=-F_{+-,++}{}^{pp}(\theta),\\
F_{-+,+-}{}^{pp}(\pi-\theta)&=-F_{+-,+-}{}^{pp}(\theta).
\end{aligned}\tag{2}$$

The last relation says that upon proton exchange $F_{+-,+-}{}^{pp}$ goes to $F_{-+,+-}{}^{pp}$ and vice versa. Finally, the sixth amplitude, $F_{-+,++}{}^{pp}(\theta)$, is equal to $\pm F_{+-,++}{}^{pp}(\theta)$ and is no longer independent. Thus, there are just five independent amplitudes. These are the same as the φ_i amplitudes of Goldberger *et al.*[13] as follows:

$$\varphi_1=F_{++,++}(\theta),\quad \varphi_2=F_{--,++}(\theta),$$
$$\varphi_5=F_{+-,++}(\theta),\quad \varphi_3=F_{+-,+-}(\theta),\quad \varphi_4=F_{-+,+-}(\theta).$$

For the np case, if the neutron and proton are considered as totally different objects, there are still six amplitudes with no relationships between $F(\pi-\theta)$ and $F(\theta)$. However, in practice, isotopic spin invariance leads to an important simplification. We regard the np system as being a sum of orthogonal $I=1$ and $I=0$ states. Here I is the total isotopic spin of the system, I_z is the component along the axis of quantization, and an isotopic spin state is represented by $|I,I_z\rangle$. The np state $|np\rangle$ is

$$|np\rangle=[|1,0\rangle+|0,0\rangle]/\sqrt{2}$$

and

$$F_{\lambda_a'\lambda_b',\lambda_a\lambda_b}{}^{np}(\theta)=\tfrac{1}{2}[F_{\lambda_a'\lambda_b',\lambda_a\lambda_b}{}^{1}(\theta)+F_{\lambda_a'\lambda_b',\lambda_a\lambda_b}{}^{0}(\theta)].\tag{3}$$

Here the superscripts 1 and 0 denote the $I=1$ state, and $I=0$ state, respectively. Of course,

$$F_{\lambda_a'\lambda_b',\lambda_a\lambda_b}{}^{pp}(\theta)=F_{\lambda_a'\lambda_b',\lambda_a\lambda_b}{}^{1}(\theta).$$

The generalized Pauli principle applied to the $I=0$ amplitudes gives relations like those of Eq. (1), but with opposite sign. The relations can be combined to be

$$\begin{aligned}
F_{++,++}{}^{I}(\pi-\theta)&=-(-1)^I F_{++,++}{}^{I}(\theta),\\
F_{--,++}{}^{I}(\pi-\theta)&=-(-1)^I F_{--,++}{}^{I}(\theta),\\
F_{+-,++}{}^{I}(\pi-\theta)&=(-1)^I F_{+-,++}{}^{I}(\theta),\\
F_{-+,+-}{}^{I}(\pi-\theta)&=(-1)^I F_{+-,+-}{}^{I}(\theta).
\end{aligned}\tag{4}$$

For $I=0$ as for $I=1$, there are only five independent amplitudes. Therefore, counting both $I=1$ and $I=0$, the nucleon-nucleon system has 10 independent amplitudes. To find these 10 amplitudes, it is not only necessary to make differential cross-section and polarization measurements on the pp and np systems, but double and triple scattering experiments are also necessary.[5] For the pp system at the high energies of interest here, only differential cross-section measurements and some polarization measurements have been done. For the np system we only have differential cross-section measurements of which this experiment was the first above 1 GeV. Therefore, the complete set of amplitudes cannot be determined now.

In particular, the differential cross section $(d\sigma/d\Omega)$ only gives sums of the squares of amplitudes as follows:

$$\begin{aligned}
(d\sigma/d\Omega)^{pp}=&\tfrac{1}{2}|F_{++,++}{}^{1}(\theta)|^2+\tfrac{1}{2}|F_{--,++}{}^{1}(\theta)|^2\\
&+2|F_{+-,++}{}^{1}(\theta)|^2+\tfrac{1}{2}|F_{+-,+-}{}^{1}(\theta)|^2\\
&+\tfrac{1}{2}|F_{-+,+-}{}^{1}(\theta)|^2,
\end{aligned}\tag{5}$$

$$\begin{aligned}
(d\sigma/d\Omega)^{np}=&\tfrac{1}{8}|F_{++,++}{}^{1}(\theta)+F_{++,++}{}^{0}(\theta)|^2\\
&+\tfrac{1}{8}|F_{--,++}{}^{1}(\theta)+F_{--,++}{}^{0}(\theta)|^2\\
&+\tfrac{1}{2}|F_{+-,++}{}^{1}(\theta)+F_{+-,++}{}^{0}(\theta)|^2\\
&+\tfrac{1}{8}|F_{+-,+-}{}^{1}(\theta)+F_{+-,+-}{}^{0}(\theta)|^2\\
&+\tfrac{1}{8}|F_{-+,+-}{}^{1}(\theta)+F_{-+,+-}{}^{0}(\theta)|^2.
\end{aligned}\tag{6}$$

Note that in the np case, in each bracket the F^1 and F^0 amplitudes have opposite symmetries about $\theta=\pi/2$.

There is another way to describe the nucleon-nucleon scattering amplitudes which started as a low-energy formalism but can be used at any energy.[13] This formalism classifies the initial and final states by the total angular momentum J, the orbital angular momentum L, the singlet or triplet nature of the total spin S ($S=0$ or $S=1$), and the z component of the total angular momentum m. The classification scheme which is quite well known is given below for the pp (or $I=1$) state. It is based on the Pauli-principle requirement

---

[13] For further explanation of the helicity amplitudes used in this paper, see M. L. Goldberger, M. T. Grisaru, S. W. MacDowell, and D. Y. Wong, Phys. Rev. **120**, 2250 (1960). For further explanation of the $M_{ij}(\theta)$ amplitudes used in this paper, see H. P. Stapp, T. J. Ypsilantis, and N. Metropolis, *ibid.* **105**, 302 (1957), and references therein. For relations between either of these sets of amplitudes and the Regge model, see W. Rarita, R. Riddell, Jr., C. Chiu, and R. J. N. Phillips, *ibid.* **165**, 1615 (1968); H. A. Neal and B. Young, Nuovo Cimento Letters **1**, 369 (1969).

that the total space-spin state must be antisymmetric in the two protons.

Singlet state	Triplet state
The spin state is antisymmetric and the space state symmetric; therefore, L is even. For $J=L$ (only case), J is even.	The spin state is symmetric and the space state antisymmetric; therefore, L is odd. For $J=L\pm1$, J is even. For $J=L$, J is odd.

Since J and parity are conserved in the scattering, there are no transitions between the singlet or triplet states. The allowed independent amplitudes are five in number as follows:

$$\begin{array}{lll} \text{Singlet state,} & J \text{ even } (L=J, m) & \leftrightarrow (L=j, m) \\ \text{Triplet state,} & J \text{ odd } (L=J, m) & \leftrightarrow (L=J, m) \\ & J \text{ even } (L=J+1, m) & \leftrightarrow (L=J+1, m) \\ & J \text{ even } (L=J-1, m) & \leftrightarrow (L=J-1, m) \\ & J \text{ even } (L=J+1, m) & \leftrightarrow (L=J-1, m) \end{array}$$

It has become usual to use amplitudes of the form $M_{ij}(\theta)$, where the singlet-state transition is denoted by $i=s$, $j=s$, namely, $M_{ss}(\theta)$, and the triplet-state transitions by $i=+1, 0, -1$; $j=+1, 0, -1$. Although there are only four independent triplet-state amplitudes, it has also been customary to use five, namely: $M_{00}(\theta)$, $M_{11}(\theta)$, $M_{01}(\theta)$, $M_{10}(\theta)$, and $M_{1-1}(\theta)$, keeping in mind that there is a relation between them. We also add the superscript 0 or 1 to designate the $I=0$ or $I=1$ states.

The differential cross-section formulas equivalent to Eqs. (5) and (6) are[13]

$$\begin{aligned} (d\sigma/d\Omega)^1 &= \tfrac{1}{4}|M_{ss}{}^1|^2+\tfrac{1}{4}|M_{00}{}^1|^2+\tfrac{1}{2}|M_{11}{}^1|^2 \\ &\quad +\tfrac{1}{2}|M_{10}{}^1|^2+\tfrac{1}{2}|M_{01}{}^1|^2+\tfrac{1}{2}|M_{1-1}{}^1|^2, \\ (d\sigma/d\Omega)^{np} &= \tfrac{1}{16}|M_{ss}{}^1+M_{ss}{}^0|^2+\tfrac{1}{16}|M_{00}{}^1+M_{00}{}^0|^2 \\ &\quad +\tfrac{1}{8}|M_{11}{}^1+M_{11}{}^0|^2+\tfrac{1}{16}|M_{10}{}^1+M_{10}{}^0|^2 \\ &\quad +\tfrac{1}{8}|M_{01}{}^1+M_{01}{}^0|^2+\tfrac{1}{8}|M_{1-1}{}^1+M_{1-1}{}^0|^2. \end{aligned} \tag{7}$$

The amplitudes $M_{ss}{}^1$, $M_{01}{}^1$, and $M_{10}{}^1$ are symmetric about $\theta=\pi/2$, and $M_{00}{}^1$, $M_{11}{}^1$, and $M_{1-1}{}^1$ are antisymmetric about $\theta=\pi/2$. The $M_{ij}{}^0$ amplitudes have just the opposite symmetry.

From Eqs. (6) and (7), we see that the expression $[(d\sigma/d\Omega)^{np}(\theta)+(d\sigma/d\Omega)^{np}(\pi-\theta)]$ contains terms like $[M_{iz}{}^1(\theta)M_{iz}{}^0(\theta)+M_{iz}{}^1(\pi-\theta)M_{iz}{}^0(\pi-\theta)]$ which cancel, since $M_{iz}{}^1$ and $M_{iz}{}^0$ have opposite symmetry about $\theta=\pi/2$. With this consideration,

$$\begin{aligned} (d\sigma/d\Omega)^0(\theta) &= 2[(d\sigma/d\Omega)^{np}(\theta)+(d\sigma/d\Omega)^{np}(\pi-\theta)] \\ &\quad -(d\sigma/d\Omega)^{pp}(\theta). \end{aligned} \tag{8}$$

Thus, from the combined pp and np data, one can find the differential cross section

$$\begin{aligned} (d\sigma/d\Omega)^0(\theta) &= \tfrac{1}{4}|M_{ss}{}^0|^2+\tfrac{1}{4}|M_{00}{}^0|^2+\tfrac{1}{2}|M_{11}{}^0|^2 \\ &\quad +\tfrac{1}{2}|M_{10}{}^0|^2+\tfrac{1}{2}|M_{01}{}^0|^2+\tfrac{1}{2}|M_{1-1}|^2, \end{aligned} \tag{9}$$

where $(d\sigma/d\Omega)^0(\theta)$ is the differential cross section for the $I=0$ state, a state not physically obtainable.

In the diffraction region, of the two guides to evaluating the different amplitudes, the optical model and the Regge model, the optical model is not very useful because it is not designed to consider the spin-flip or helicity-flip amplitudes in a detailed way. The Regge model allows detailed specific separate amplitude calculations, but these, in turn, depend upon the selection of a set of trajectories.[13] For the nucleon-nucleon case, five trajectories are usually considered, namely, those corresponding to the two vacuum poles P and P', and to the ρ meson, ω meson, and A_2 meson; and a helicity amplitude is, in general, the sum of five amplitudes:

$$F_{\lambda_a'\lambda_b',\lambda_a\lambda_b}(\theta)=\sum_{T=P,P',\rho,\omega,A_2} F_{\lambda_a'\lambda_b',\lambda_a\lambda_b,T}(\theta).$$

In the separate-trajectory helicity amplitudes, the sign is the same for the P, P', and ω in pp and np, but it changes for the ρ and A_2. Therefore, if there is a difference between pp and np scattering in the diffraction region, it must be ascribed, in the Regge theory, to the presence of ρ or A_2 trajectories. The presence of the ρ and A_2 could only be detected in the diffraction region, where the behavior of the trajectory is hopefully a simple function of t. Now, evidence from total cross-section measurements and np charge exchange indicates that the present pp data can be fitted with the ρ and A_2 trajectories neglected.[13] This assumption, together with the simplifications

$$\begin{aligned} F_{++,++}{}^I(\theta) &= F_{-+,-+}{}^I(\theta), \\ F_{+-,++}{}^I(\theta) &= F_{-+,++}{}^I(\theta), \end{aligned} \tag{10}$$

constitutes the most recent conditions used to fit pp and other hadron-hadron scattering. On the other hand, if we find a substantial difference between pp and np in the diffraction region, this will require use of the ρ or A_2 trajectory, although the profusion of amplitudes will prevent definite location of these contributions.

We next consider the large-angle region. At $\theta=\pi/2$, there is a simplification in the amplitudes. Clearly, all antisymmetric amplitudes must be zero. Thus,

$$\begin{gathered} M_{00}{}^1(\pi/2)=0, \quad M_{11}{}^1(\pi/2)=0, \\ M_{1-1}{}^1(\pi/2)=0, \quad M_{ss}{}^0(\pi/2)=0, \\ M_{01}{}^0(\pi/2)=0, \quad M_{10}{}^0(\pi/2)=0. \end{gathered} \tag{11}$$

In terms of helicity amplitudes,

$$\begin{gathered} F_{++,++}{}^0(\pi/2)=0, \quad F_{--,++}{}^0(\pi/2)=0, \\ F_{+-,++}{}^1(\pi/2)=0, \\ F_{+-,+-}{}^1(\pi/2)=-F_{-+,+-}{}^1(\pi/2), \\ F_{+-,+-}{}^0(\pi/2)=+F_{-+,+-}{}^0(\pi/2). \end{gathered} \tag{12}$$

If these relations are inserted in Eqs. (7) or (6), respectively, it is immediately found that

$$(d\sigma/d\Omega)^{pp}(\pi/2)\leq 4(d\sigma/d\Omega)^{np}(\pi/2). \tag{13}$$

This inequality has been known for a long time[14] and is a consequence of the isotopic spin concept. If it is violated by experiment, then to regard the neutron and proton as an isotopic doublet is wrong. It has been shown to be true at energies below 1 GeV, and, as we shall see below, our data indicate that this inequality is well satisfied below 7 GeV/*c*.

Further reduction of the number of amplitudes depends upon physical assumptions. One assumption is that all $M_{iz}{}^{I}$ amplitudes which have $i\neq z$ are zero at and near $\pi/2$. This says that the z component of S, the total spin, cannot change. This concept can be justified if the large-angle scattering interaction can be regarded as due to a central force. With the *central-force assumption*, only $M_{ss}{}^{I}(\theta)$, $M_{00}{}^{I}(\theta)$, and $M_{11}{}^{I}(\theta)$ are nonzero. This, combined with restrictions of Eq. (11), yields

$$\begin{aligned}(d\sigma/d\Omega)^{pp}(\pi/2)&=\tfrac{1}{4}|M_{ss}{}^{1}(\pi/2)|^{2},\\ (d\sigma/d\Omega)^{np}(\pi/2)&=\tfrac{1}{16}|M_{ss}{}^{1}(\pi/2)|^{2}\\ &\quad+\tfrac{1}{16}|M_{00}{}^{0}(\pi/2)|^{2}+\tfrac{1}{8}|M_{11}{}^{0}(\pi/2)|^{2}.\end{aligned}\tag{14}$$

The assumption of no helicity flip, on the other hand, leads to different results because then only $F_{++,++}{}^{I}(\theta)$ and $F_{-+,-+}{}^{I}(\theta)$ are nonzero. At $\theta=\pi/2$, using Eq. (12), one has

$$\begin{aligned}(d\sigma/d\Omega)^{pp}(\pi/2)&=\tfrac{1}{2}|F_{++,++}{}^{1}(\pi/2)|^{2}+\tfrac{1}{2}|F_{+-,+-}{}^{1}(\pi/2)|^{2},\\ (d\sigma/d\Omega)^{np}(\pi/2)&=\tfrac{1}{8}|F_{++,++}{}^{1}(\pi/2)|^{2}+\tfrac{1}{8}|F_{+-,+-}{}^{1}(\pi/2)|^{2}.\end{aligned}$$

Thus, no helicity flip at $\pi/2$ requires the equality

$$(d\sigma/d\Omega)^{pp}(\pi/2)=4(d\sigma/d\Omega)^{np}(\pi/2).\tag{15}$$

But no change of the z of component of S (S_z) requires only an inequality

$$(d\sigma/d\Omega)^{pp}(\pi/2)\leq 4(d\sigma/d\Omega)^{np}(\pi/2),\tag{16}$$

the same inequality as Eq. (13).

When one considers the values of $(d\sigma/d\Omega)^{np}$ in the neighborhood of $\theta=\pi/2$, there are still some observations which can be made by comparing $(d\sigma/d\Omega)^{np}(\theta)$ with $(d\sigma/d\Omega)^{np}(\pi-\theta)$. Using Eqs. (7) and (8), one can write

$$\begin{aligned}(d\sigma/d\Omega)^{np}(\theta)&=\tfrac{1}{4}(d\sigma/d\Omega)^{1}(\theta)+\tfrac{1}{4}(d\sigma/d\Omega)^{0}(\theta)\\ &\quad+(\text{interference term}).\end{aligned}\tag{17}$$

The interference term is antisymmetric about $\theta=\pi/2$ because it is the sum of terms, each of which is a product of a symmetric and an antisymmetric amplitude. Therefore, the symmetry of $(d\sigma/d\Omega)^{np}$ about $\theta=\pi/2$ is a test of the importance of the interference term. Since the diffraction peak in *np* scattering is so much larger than the *np* backward (charge-exchange) scattering peak, there must be a strong interference in all the pairs of amplitudes for θ close to 0. Thus, in terms of $F_{\lambda_a'\lambda_b',\lambda_a\lambda_b}(\theta)$ amplitudes, a simple model for small θ would be to set all the helicity-flip amplitudes equal to zero. Then for θ *small*,

$$\begin{aligned}(d\sigma/d\Omega)^{pp}(\theta)&\approx\tfrac{1}{2}|F_{++,++}{}^{1}(\theta)|^{2}+\tfrac{1}{2}|F_{+-,+-}{}^{1}(\theta)|^{2},\\ (d\sigma/d\Omega)^{np}(\theta)&\approx\tfrac{1}{8}|F_{++,++}{}^{1}(\theta)+F_{++,++}{}^{0}(\theta)|^{2}\\ &\quad+\tfrac{1}{8}|F_{+-,+-}{}^{1}(\theta)+F_{+-,+-}{}^{0}(\theta)|^{2}.\end{aligned}\tag{18}$$

The strong interference is obtained by setting

$$\begin{aligned}F_{++,++}{}^{1}(\theta)&\approx F_{++,++}{}^{0}(\theta)\quad\text{for }\theta\ll\pi/2,\\ F_{+-,+-}{}^{1}(\theta)&\approx F_{+-,+-}{}^{0}(\theta)\quad\text{for }\theta\ll\pi/2.\end{aligned}\tag{19}$$

Then

$$(d\sigma/d\Omega)^{np}(\theta)=(d\sigma/d\Omega)^{pp}(\theta),$$

and

$$(d\sigma/d\Omega)^{np}(\pi-\theta)\approx 0.$$

We conclude this section with brief discussions of several theories of nucleon-nucleon elastic scattering in the 90° region. All these theories have in common the recognition of the fact that there are too many amplitudes for exact calculations and that general considerations must be found which allow either neglecting or summing over sets of amplitudes. These theories are generally concerned with the relation of *pp*, *np*, and $\bar{p}p$ differential cross sections in the 90° region and in predicting the behavior of these cross sections as a function of t or θ.

The first attempt to understand large-angle nucleon-nucleon scattering was the statistical model of Fast, Hagedorn, and Jones.[15] This model has since been considerably elaborated upon by Hagedorn.[16] In the simpler form of this model, the *np* differential cross section is taken to be isotropic in the region of 90°, so that $(d\sigma/d\Omega)^{np}$ should be flat as a function of $\cos\theta$ in that region. The simple model also predicts that the cross section near 90° should fall off with energy as given in

$$(d\sigma/d\Omega)^{np}(\pi/2)=\sigma_{\text{inel}}/4p^{*2}e^{h(E+g)}.\tag{20}$$

Here σ_{inel} is the total *np* inelastic cross section, g and h are constants, E is the total energy, and p^* is the momentum in the barycentric system.

Sisakyan *et al.*[17] have recently reconsidered the statistical model with respect to comparing the *pp*, *np*, and $\bar{p}p$ differential cross sections at 90°. They predict that the *pp* and *np* cross sections should be about equal, but that the $\bar{p}p$ cross section should be smaller by a factor of 1/500 above laboratory energies of 8 or 9 GeV. Furthermore, this factor should be constant as the energy increases further.

The major difficulty of the simple statistical model is that it predicts isotropic differential cross section about 90° even for $\bar{p}p$ scattering, where the experiments definitely show a constantly falling cross section. Such

---

[14] D. Feldman, Phys. Rev. **89**, 1159 (1953).

[15] H. Fast, R. Hagedorn, and L. W. Jones, Nuovo Cimento **27**, 856 (1963).

[16] R. Hagedorn, Nuovo Cimento **15**, 434 (1960).

[17] I. N. Sisakyan, E. L. Feinberg, and D. S. Chernavskii, Zh. Eksperim. i Teor. Fiz. Pis'ma v Redaktsiyu **4**, 432 (1966) [English transl.: JETP Letters **4**, 290 (1966)].

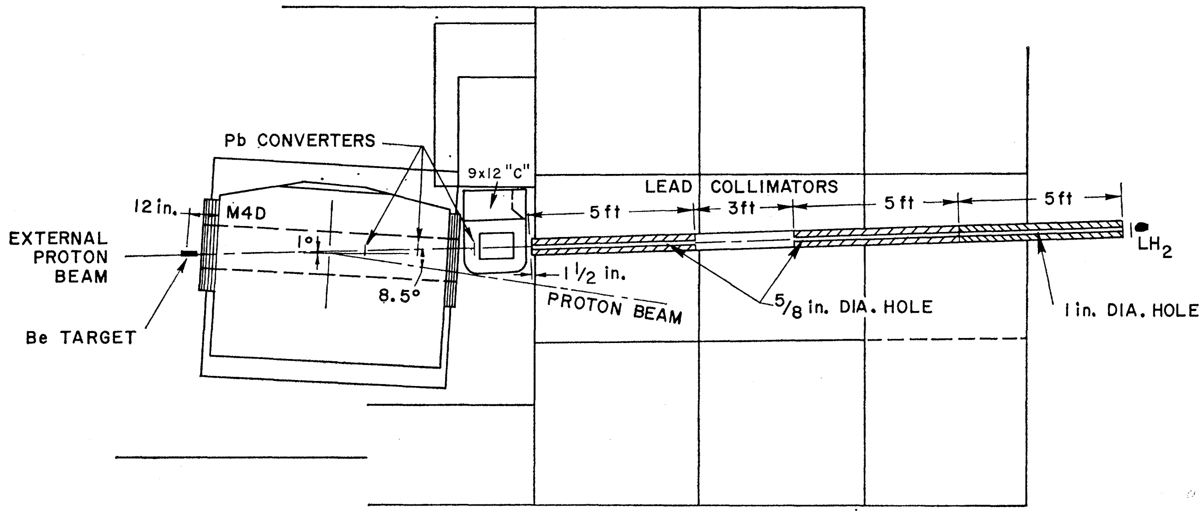

FIG. 1. The neutron beam.

considerations led Bialas and Czyzewski[18] to discard the statistical model in favor of a theory which looks upon np and $\bar{p}p$ elastic scattering as being the sum of direct elastic and charge-exchange elastic processes. The direct elastic processes are regarded as the same for pp, np, and $\bar{p}p$; and interferences between the two types of processes are neglected. The reader is referred to the original paper for details. We just mention two of their conclusions. For $\theta<90°$, pp and np elastic scattering should be similar in shape, but for np scattering at $\theta>90°$, the dominating process is charge-exchange elastic scattering which can behave in a completely different manner from direct elastic scattering.

In a series of papers, Kastrup[19,20] has developed a theory of nucleon-nucleon elastic scattering which uses the concept of soft-pion emission, in analogy to bremsstrahlung, to explain the rapid decrease of the differential cross section with t. He is able to make specific predictions about the energy behavior of $(d\sigma/d\Omega)$ and to reduce the consideration of pp and np scattering in the 90° region to the consideration of two general isospin amplitudes, the interference between which is allowed to be adjusted. Again, the reader is referred to the original paper for the detailed theory.

Wu and Yang[21] have devoted considerable thought to the pp and np 90° region. They independently predicted symmetry in the np cross sections about $\theta=\pi/2$. They argue that the rapid falloff of the differential cross sections as $|t|$ (the four-momentum transfer) increases in hadron-nucleon collisions is explained by picturing the nucleon as an extended object held together with an internal rigidity of a few hundred MeV. The falloff with increasing $|t|$ is attributed to the difficulty of accelerating this extended object without "breaking it up" and producing an inelastic final state. They then use the concept of Krisch[22] and Orear[23] that the momentum transfer in the *barycentric system* can be divided into components perpendicular to and parallel to the line of collision. Thus, $|t|=p_\perp^{*2}+p_{\parallel}^{*2}$. Next they argue that in a $\theta>\pi/2$ collision, one can regard the neutron as *exchanging charge* with the proton and, thus, that the collision can be treated as a $(\pi-\theta)<\pi/2$ collision. This concept that the neutron and proton exchange charge easily means that $p_{\parallel}$ cannot be important in the collision, that the cross section only depends on $p_\perp^*$, and, thus, that the cross section is symmetric about 90°. Of course, this concept cannot be extended to small angles because there it contradicts experimental results.

Wu and Yang further assume that in a large-angle collision there are many final states available to the nucleons and that there is no strong energy dependence in the choice of the final state. This assumption and their interpretation of the role of $p_\perp$ leads to the prediction that in the limit of very high energies, cross sections for different reactions that involve the same $p_\perp$ should appear quite similar. In particular, it is predicted that at large angles

$$\lim_{S\to\infty}\frac{\ln d\sigma/d\Omega(\theta,\,np\to np)}{\ln d\sigma/d\Omega(\theta,\,pp\to pp)}\to 1\,, \qquad (21)$$

$$\lim_{S\to\infty}\frac{\ln d\sigma/d\Omega(\theta,\,np\to np)}{d\sigma/d\Omega(\pi-\theta,\,np\to np)}\to 1\,. \qquad (22)$$

Wu and Yang make another prediction about large-angle scattering. It is assumed that the elastic differential cross sections in different isotopic spin channels have, on the average, the same absolute amplitudes and random relative phases. Thus, if $M_{iz}{}^{I}$ is the matrix

---

[18] A. Bialas and O. Czyzewski, Nuovo Cimento **49A**, 273 (1967).

[19] H. A. Kastrup, Phys. Rev. **147**, 1130 (1966).

[20] H. A. Kastrup, Nucl. Phys. **B1**, 309 (1967).

[21] T. T. Wu and C. N. Yang, Phys. Rev. **137**, B708 (1965).

[22] A. D. Krisch, Phys. Rev. Letters **11**, 217 (1963).

[23] J. Orear, Phys. Rev. Letters **12**, 112 (1964).

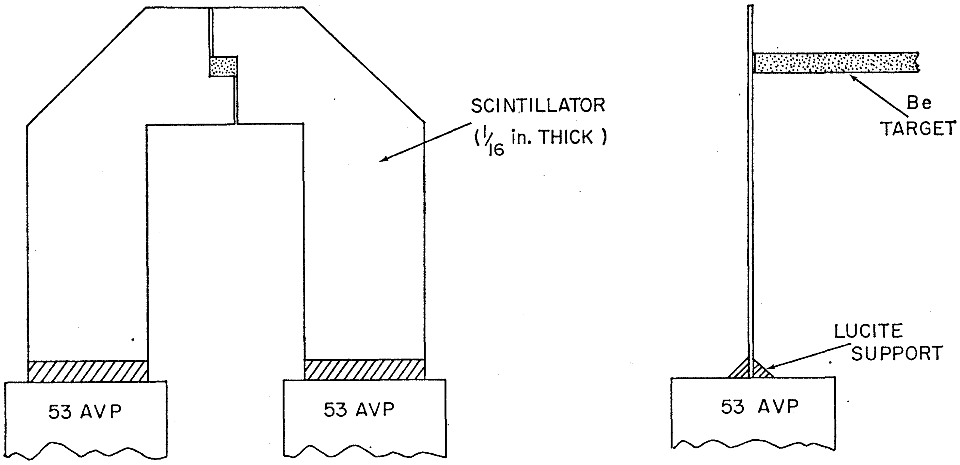

FIG. 2. Beam position monitors. The scintillation counters framed the upstream end of the beryllium target.

element for a scattering process with total isotopic spin I, then on the average

$$M_{iz}{}^{I}M_{iz}{}^{I'}=\delta_{II'}(M_{iz}{}^{1})^{2}. \qquad (23)$$

From Eq. (7), using Eq. (23) for angles near $\theta=\pi/2$, one has

$$(d\sigma/d\Omega)^{pp}=\tfrac{1}{4}|M_{ss}{}^{1}|^{2}+\tfrac{1}{4}|M_{00}{}^{1}|^{2}+\cdots,$$
$$(d\sigma/d\Omega)^{np}=\tfrac{1}{8}|M_{ss}{}^{1}|^{2}+\tfrac{1}{8}|M_{00}{}^{1}|^{1}+\cdots.$$

Thus, with these assumptions $(d\sigma/d\Omega)^{pp}=2(d\sigma/d\Omega)^{np}$. This Wu-Yang prediction for the 90° region is different from their other predictions in Eqs. (21) and (22).

III. EXPERIMENTAL DETAILS

A. Neutron Beam

The neutron beam for this experiment was produced by focusing a proton beam onto a beryllium target, sweeping away the charged particles, and then collimating the neutrons into a beam well-defined spatially, but with a very broad energy spectrum. The experiment was performed using the external proton beam of the Bevatron at the Lawrence Radiation Laboratory. This beam was ejected from the main ring during a 300-msec flattop pulse and yielded a spill of 6.3-GeV protons every 6 sec. During the course of the experiment, the intensity in the external beam varied between 1 and 7×10^{10} protons per pulse.

As shown in Fig. 1, the proton beam was focused onto a beryllium target $\frac{3}{8}$-in.×$\frac{1}{4}$-in. in cross section and 8 in. (about $\frac{2}{3}$ collision lengths) long. The position of the proton beam on the beryllium target was monitored with two independent systems. A closed-circuit television camera, looking at a thin piece of plastic scintillator placed directly upstream of the Be target, gave a visual indication of the location of the beam spot. Special monitor counters were also used. As shown in Fig. 2, these counters were $\frac{1}{16}$-in. scintillators framing the upstream end of the Be target. By observing the output of these two tubes on an oscilloscope it was possible to detect drifts of the position of the proton beam of the order of $\frac{1}{16}$ in. The Be target itself was mounted on a hinge attached to the first bending magnet. The hinge allowed easy removal and accurate replacement of the target whenever a check of the alignment of the beam was necessary.

Immediately following the Be target, a large sweeping magnet, M4D, removed charged particles from the beam. M4D, an 84-in. long, 15-in. wide, 4-in. bending magnet, was run at a nominal current of 1000 A ($B=14$ kG) to bend the unscattered proton beam through 8.5°. Because M4D served no analyzing function, its alignment was not critical.

The photon contamination in the neutron beam was reduced with three pieces of $\frac{1}{4}$-in. lead (a total of 3.8 radiation lengths), followed by a small 9-in.×12-in. "C" magnet to sweep out the electron pairs. The lead converter was divided into three sections to increase the efficiency of the system in removing γ rays.

At 15 ft from the center of the Be target, the neutrons entered the first of three lead collimators. Two 5-ft long pieces of 12-in.×3-in. steel channel were welded to form a rectangular tube. A steel pipe was supported in the center of the tube by bars on each end, and the entire tube except for the inside of the pipe was filled with 1575 lb of lead. The first two of these units had pipes of $\frac{5}{8}$-in. i.d., while the third had a pipe with a 1-in. inside diameter.

The central ray of the neutrons entering the collimators made an angle of 1° with respect to the original proton beam. This angle was selected because a preliminary survey experiment showed that the neutron flux is greatest at small production angles; safety precautions, however, prohibited angles smaller than 1°. As shown in Fig. 1, the proton beam was swept to the opposite side of the 0° line so that at the entrance of the collimator, the neutron beam and the charged particles were separated by 1.1 ft. The solid angle subtended by the collimator system was determined by

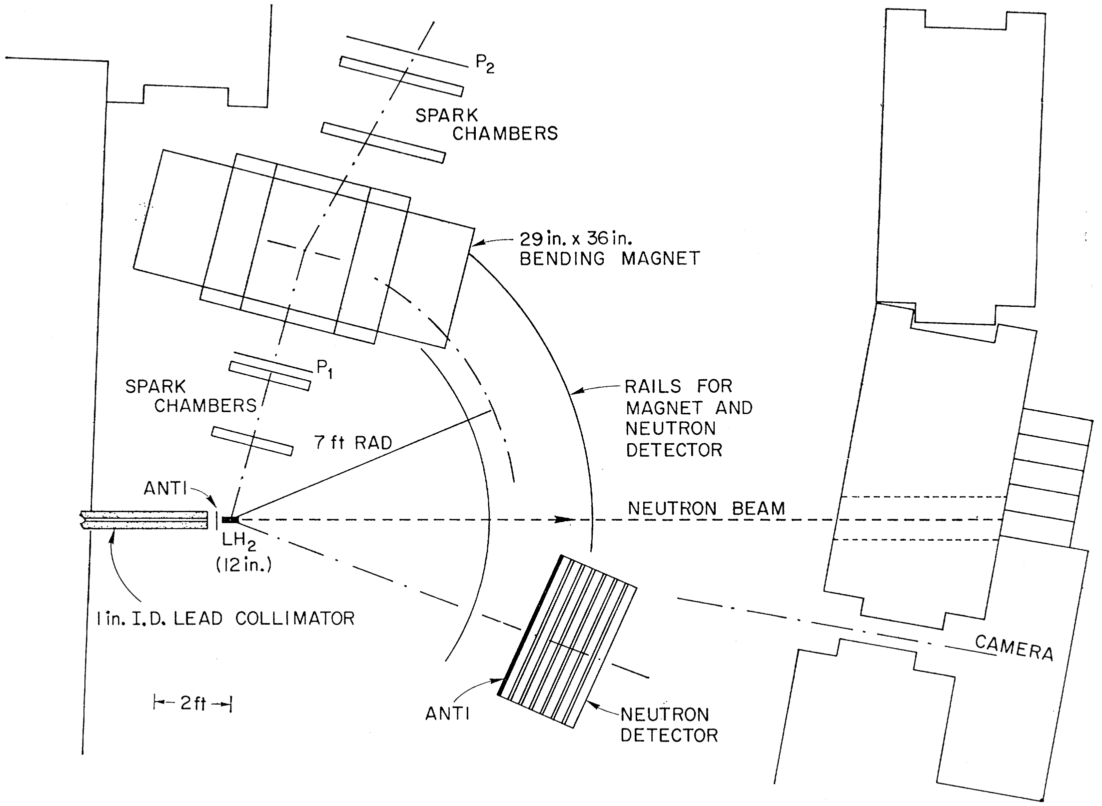

FIG. 3. Plan view of the main experimental area showing the liquid hydrogen target, proton spectrometer, and neutron detector.

the downstream end of the second collimator and was 3.87×10^{-6} sr. As the beam was defined by the first two collimators, the larger diameter of the third unit of the collimator system reduced the number of neutrons in the beam that had scattered against the sides of the collimators.

The shielding wall in which the collimators were embedded was designed to minimize the neutron backgrounds in the main experimental area. The wall consisted of 5 ft of steel followed by 10 ft of heavy concrete. All crevices between the blocks of steel and concrete were filled with lead bricks and lead shot.

When the neutron beam left the collimator, it was roughly 1 in. in diam, with negligible spatial tails and an angular divergence of less than 0.15°. The energy spectrum of the neutrons was determined from the analysis of elastic scattering events and will be discussed later.

B. Hydrogen Target

Three main considerations determined the design of the target: (1) that a minimum amount of material other than hydrogen should be present in the path of the beam; (2) that there should be no unnecessary material for the scattered particles to pass through for 90° on either side of the beam line; and (3) that all material other than hydrogen in the beam's path be far enough from the hydrogen region to permit a clean separation of interactions in the material from interactions in the hydrogen. Therefore, the fill lines and vent lines to the Mylar flask that contained the hydrogen were arranged so that they did not obstruct the beam. In addition, the vacuum jacket leading back to the reservoir was set an angle so that there was a clear view of the flask for 90° on either side of the beam line.

The neutron beam entered the hydrogen target vacuum jacket surrounding the flask through a 0.020-in.-thick Mylar entrance window. The hydrogen was contained in a 10-in.-long Mylar cylinder with domes on either end, yielding a flask 12 in. long and $\frac{5}{2}$ in. in diam with 0.005-in. thick walls. The flask was wrapped with 10 layers of aluminized Mylar (0.00025 in. thick) and aluminum foil (0.00025 in. thick) to reduce heat transfer by radiation. The aluminum vacuum jacket was a $15\frac{1}{4}$-in.-long domed cylinder, 8 in. in diam, with 0.040-in.-thick walls. The flask was centered in the vacuum jacket, thereby allowing at least $\frac{5}{2}$ in. between the flask and the vacuum jacket or the entrance window.

Target-empty runs were made during the experiment and it was found that the number of elastic interactions which appeared to have taken place in the 10-in.-long fiducial volume of the target was negligible.

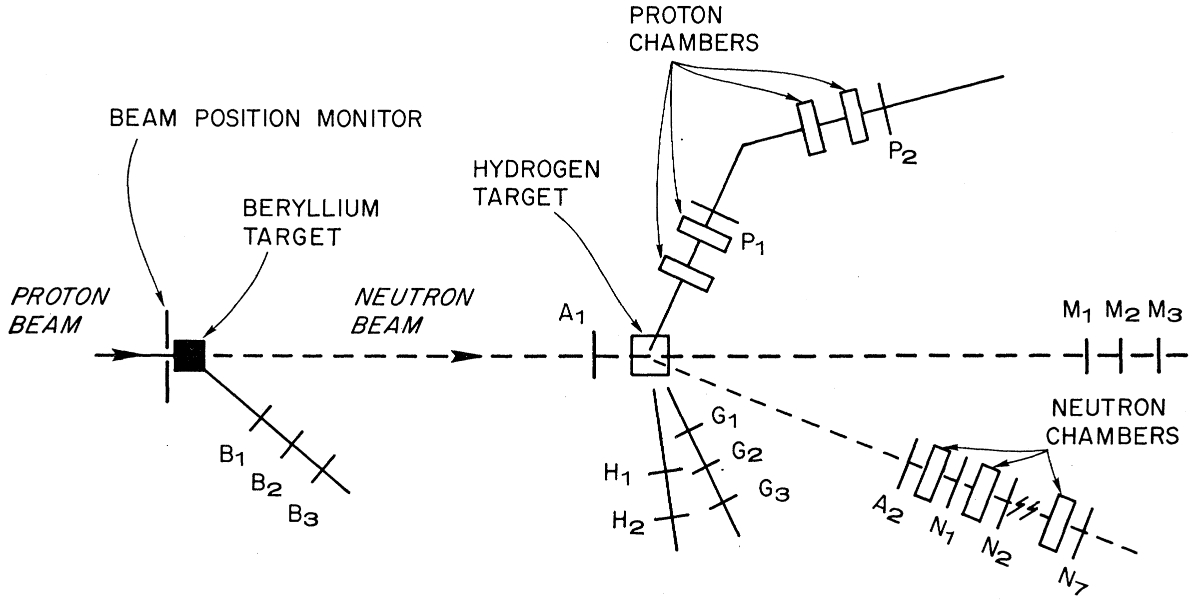

FIG. 4. Schematic diagram of scintillation counter layout.

C. Proton Spectrometer

The momentum and angle of the recoil proton were measured with two pairs of thin-plate spark chambers before and after a bending magnet. The plan view of the spectrometer is shown in Fig. 3.

The spark chambers each had four $\frac{3}{8}$-in. gaps with 1-mil aluminum foil plates. The active area of the two chambers on the target side of the magnet was 22 in. long and 6 in. high. The chambers on the other side of the magnet were 39 in. long and 11 in. high. The chambers were operated with a 90%-Ne–10%-He gas mixture.

The analyzing magnet, ATLAS, was 29 in. wide and 36 in. long with an 8-in. gap. Very extensive measurements of the magnetic field were made by the LRL Magnet Test Group using Rawson probes and a motor-driven system. The field was measured in a 1-in. grid pattern (2800 points per grid) at seven elevations (0 in.$\pm$2.0 in., $\pm$2.8 in., and $\pm$3.0 in. from the median plane) and at six current levels ($I=392$, 588, 855, 960, 1084, and 1203 A). These data were placed on magnetic tape and used in determining the proton momentum from the position of the tracks in the spark chambers.

The magnet spark-chamber system was supported on a carriage that rode on curved railroad tracks. The tracks, centered on the liquid-hydrogen target, had radii of approximately 6 ft 4 in. and 9 ft 7 in. The center of the magnet system rode 7 ft from the center of the target. The support system contained provisions for rotating the magnet and adjusting its height in order to align the magnet system after its position on the rails had been changed. At each setting of the system there was roughly a 12° acceptance interval for recoil protons. For low-momentum protons, knowledge of the proton angle was limited primarily by multiple Coulomb scattering in the hydrogen and in the vacuum jacket. The momentum measurements were also limited by multiple Coulomb scattering to a few precent.

D. Neutron Detector

The scattered neutron was observed by requiring that a neutral particle interact and produce at least one charged particle in an array of seven steel-plate spark chambers. The location of the point of interaction and the position of the liquid-hydrogen target yielded the angle of the scattered neutron.

The neutron detector chambers had four $\frac{3}{8}$-in. gaps with plates made from $\frac{3}{16}$-in.-thick cold-rolled stainless steel polished to a near-mirror finish. They were constructed by sandwiching frames of Lucite between the plates. The active area of each chamber was 12 in. high and 48 in. long.

The array of seven chambers represented a total of 1.4 collision lengths; therefore, roughly 60% of the neutrons that entered the detector interacted to produce charged particles. Measurement of the tracks of these particles gave the vertex of the interaction. With this vertex and the intersection of the neutron beam with the path of the recoil proton projected into the hydrogen target, the angle of the scattered neutron could be found. The accuracy of measurement of this angle was, for the most part, limited by the width of the beam in the hydrogen, and there was a typical uncertainty of $\pm$9 mrad.

This spark-chamber array also ran on the railroad tracks on a carriage 9 ft from the target. As with the magnet system, there were provisions for rotating and leveling the array to ensure alignment. At each setting

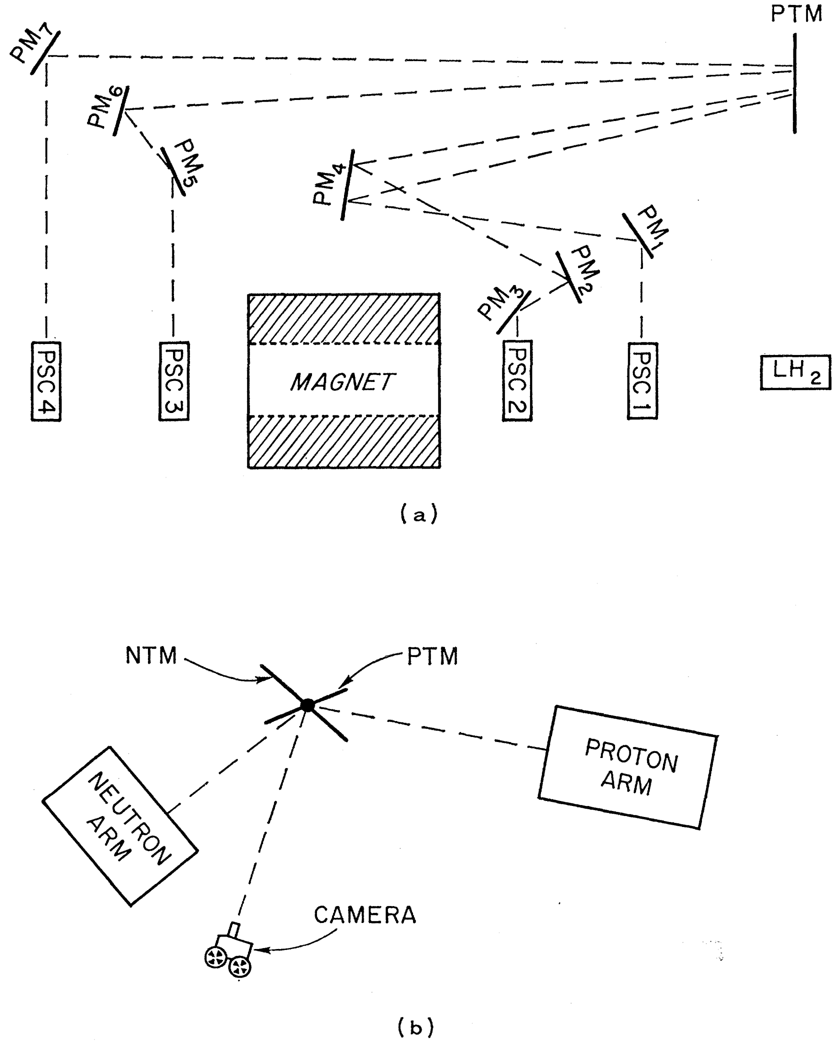

FIG. 5. Mirror System. (a) Mirrors used for proton arm; (b) mirrors located over hydrogen target used to transport light to the camera.

of the apparatus, there was a 30° acceptance interval for scattered neutrons.

During the course of the experiment the two carriages were placed in seven different settings to cover all scattering angles except the region near 180° (i.e., the charge-exchange region). When this region was reached, the scattered neutron did not have sufficient kinetic energy to produce charged particles that would trigger the detector (170 MeV was the cutoff).

E. Scintillation Counters and Electronic Logic

There were eleven scintillation counters involved in the triggering system: two in the proton arm, seven in the neutron arm, and two anticoincidence counters. The position of these counters is shown schematically in Fig. 4.

A preliminary coincidence was made between P_1, P_2 (the proton arm counters), and $\bar{A}_1$, the anticoincidence counter placed upstream of the hydrogen target. The output from this circuit was split and placed in coincidence with successive pairs of N (i.e., neutron) counters (N_1–N_7) and the anticoincidence counter $\bar{A}_2$. The outputs from all six of these coincidences were added, and if a coincidence occurred in one or more of them the spark chambers were triggered.

F. Optics

The spark chambers were photographed by a system involving a complicated arrangement of mirrors. There was a mirror for each chamber that allowed both views of the chamber to be observed from above. The proton chambers had individual stereo mirrors, while all seven neutron chambers shared a common stereo mirror. A mirror above each neutron chamber brought the light to a large mirror located over the hydrogen target, which, in turn, reflected the light to the camera located outside the experimental blockhouse (see Fig. 5). The use of separate mirrors for each of the seven neutron chambers enabled equilization of the light paths for the different chambers. Because each mirror could be ad-

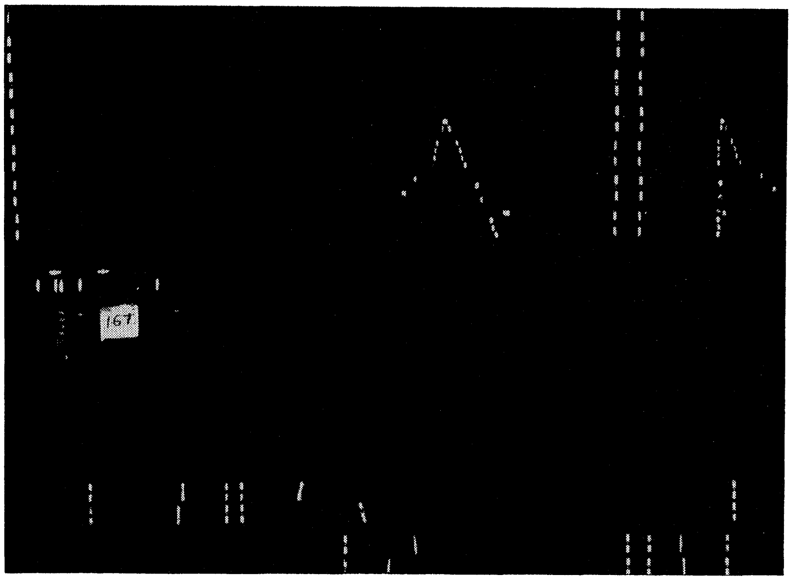

Fig. 6. A photograph from the experiment with a typical event.

justed independently, there was no need to use a field lens to view the entire active volume of each chamber.

The situation for the proton chambers was not so straightforward. To equalize the light paths and to ensure that the magnet structure did not obscure any portion of a mirror, the light paths were folded many times. The light was finally reflected into the camera by a second mirror placed over the target (see Fig. 5).

The two mirrors (PTM and NTM in Fig. 5) could be rotated around an axis perpendicular to the plane of the rail system and passing through the center of the rails. Thus, regardless of the relative positions of the neutron and proton arms, these mirrors could be adjusted to produce the same format on the film.

The information from all the spark chambers, as well as that from a data board containing the event number and run number, were recorded on one frame of 35-mm film. During the course of the experiment, approximately 600 000 pictures were taken on Eastman Linograph Shellburst film. The camera was designed[24] to take up to seven pictures during the 300-msec beam spill.

A typical picture is shown in Fig. 6 and the important features are indicated in Fig. 7. The bend in the proton's path due to the magnet can be seen, and an easily identifiable neutron interaction is present in the neutron chambers. The fiducials and the data box are also shown.

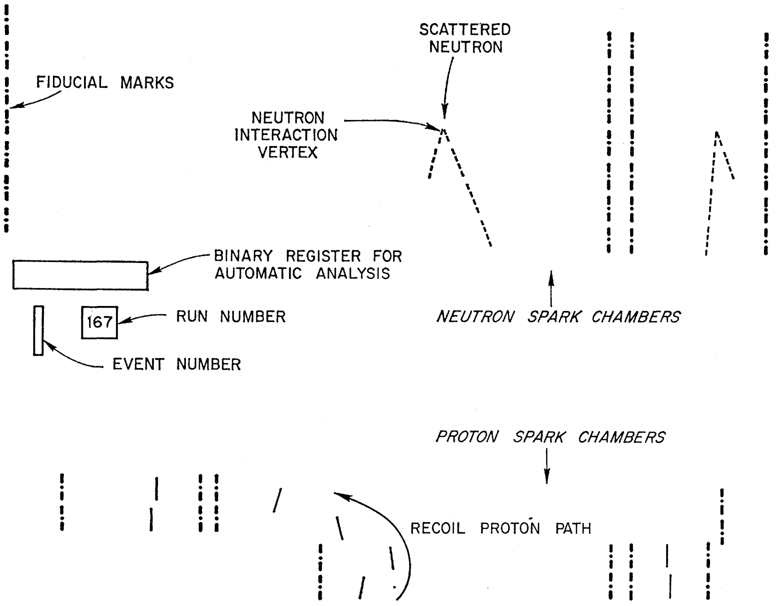

Fig. 7. Explanation of the event shown in Fig. 6, indicating the data box, the fiducials, the neutron interaction, and the bend in the proton path.

---

[24] D. E. Damouth and O. E. Haas, University of Michigan Technical Report No. 13, 1963 (unpublished).

IV. DATA REDUCTION

The film was scanned for possible elastic scattering events, and frames that satisfied all selection criteria were measured. In order for an event to be considered an elastic scattering candidate, the following criteria had to be met.

(a) All proton chambers had to have a track present and the tracks had to indicate that a positive particle had passed through the magnet. This requirement eliminated events in which the particle was negative (probably π^-) and those in which a positive particle had undergone a large-angle scatter from the pole tips or coils of the magnet.

(b) There had to be an identifiable neutron interaction or neutron star in the neutron chambers. In order to make the identification of a neutron star and its vertex more objective, the scanner had to specify also to which of five interaction-type classifications the interaction belonged.

The following measurements were made on each frame containing an event which satisfied the above criteria.

A. Three Fiducials

At the start of each frame, three fiducials were measured in order to correlate the measurements with a master fiducial grid that allowed accurate knowledge of the positions of the spark chambers. Three fiducials enabled a least-squares fit to be made which corrected for translation, rotation, and magnification.

B. Proton Sparks

In each of the four proton chambers, there were at most four sparks lying along the path of the particle. In each view of the chambers, one of these sparks was selected and the location of the center of this spark was digitized.

C. Neutron Sparks

In each of the neutron chambers, sufficient sparks on the prongs of the neutron interaction were measured to determine the location of the neutron interaction vertex. The number of prongs used and, thus, the number of sparks that had to be measured varied with the interaction type.

If there were two separate, identifiable interactions in the neutron conversion chambers, the frame was measured twice: first with one interaction and then with the other. A code in the parameter board indicated this duplication, and the χ^2 fitting program to be discussed later selected the interaction resulting in the best fit or lowest χ^2. This measurement duplication was performed to minimize any neutron-beam intensity-correlated bias in the selection process.

The efficiency for identification of neutron types and for indicating the neutron vertex correctly was measured by rescanning portions of the data. This efficiency, independent of the neutron type assigned, was found to be approximately 94%. There were, however, some disagreements regarding the neutron event classes assigned. These disagreements did not affect the measurement of the neutron vertex, however, because the interaction vertex is in the same position for all these classes. There is the worry that there might be some energy-dependent bias inherent in the scanner selection criteria or in the performance of the scanners. Measurements were made to determine the existence of such biases and were found to be unimportant.

At periodic intervals, measurements were made of the entire fiducial grid. These measurements served as checks on the performance of the measuring machines and ensured that any small change in the relative positions of the fiducials would be detected.

The events were reconstructed with an IBM 7090 computer. The measurements of the sparks on the film were transformed into real-space coordinates using a conical projection. The path of the recoil proton, determined from the coordinates of the tracks in the two spark chambers closest to the target, could be projected back into the liquid hydrogen. The interaction region in the target was limited to a 10-in.-long cylinder on the beam axis and centered in the target; therefore, the proton vector had to pass through this volume. The momentum of the recoil proton at the magnet was then calculated by an integration through the magnetic field. It was then corrected for energy loss to obtain the momentum at the interaction point. The energy losses in the scintillation counter, in the air, in the Mylar, and in the aluminum through which the proton passed were calculated using the latest tabulated values.[25] The energy loss in the liquid hydrogen was computed using a standard momentum-to-range, range-to-momentum subroutine.

A first guess at the location of the scattering point was the closest approach of the proton's path to the central ray of the incident neutron beam. The final selection of the scattering point is discussed below.

After an event had successfully gone through the kinematics program, the information about the recoil proton vector, the proton momentum, and the neutron interaction point was fed into a program closely patterned after GUTS,[26] a fitting routine commonly used in the analysis of bubble-chamber data. This program adjusted the measured quantities to give the best fit (i.e., minimum χ^2) using the method of least squares, subject to the nonlinear constraints imposed by momentum and energy conservation for elastic scattering.

The value of the minimized χ^2 was given by

$$\chi^2=\sum[(X_m{}^i-X_c{}^i)/\Delta X^i]^2,$$

where the $X_m{}^i$ are the measured quantities (proton momentum, proton angle, and neutron angle), $X_c{}^i$ are

---

[25] W. H. Barkas and M. J. Berger, NASA Report No. SP-3013, 1964 (unpublished).

[26] J. P. Berge, University of California, Alvarez Group Memo 86 (UCID-1251), 1960 (unpublished).

the calculated quantities, and the ΔX^i are the estimated uncertainties in each of the measured quantities.

The interaction point in the liquid hydrogen target which gave the best fit was found by varying the interaction point in 1-in. steps along the line determined by the proton vector. At each point inside the cylindrical interaction region the value of χ^2 was computed. The interaction point selected was that with the lowest value of χ^2.

Elastic events were then selected with the requirement that $\chi^2 \leq 8.0$. The fraction of elastic events excluded by this requirement was less than 2%.

V. CORRECTIONS TO DATA

A. Energy Dependence of Neutron Detection Efficiency

If the neutron detection efficiency were less than 100% but independent of energy, no correction to the data would be required because of the method of normalization used (see Sec. VI B). However, because of the large range of neutron scattering angles covered, it was necessary to correct for the energy dependence of the detection efficiency. This was done in the following manner.

While the apparatus was set up to measure scattering in the diffraction peak region, the triggering system was altered; the neutron counters were removed from the coincidences, so that the triggering requirement was $\bar{A}_1\bar{A}_2P_1P_2$. All the chambers were fired, therefore, whenever a charged particle passed through both proton counters in the absence of a veto from either of the two anticoincidence counters. If the assumption is made that the interaction which produced the charged particle was elastic *np* scattering, then the angle and momentum of the recoil proton are sufficient to determine all the kinematic parameters including the angle and energy of the scattered neutron (i.e., a zero-constraint fit). This assumption is justified below. One then looks in the neutron chambers for a neutron interaction at the predicted angle.

There are two considerations which make this assumption true. First the P_1P_2 counters, which were separated by 7 ft, were timed so that slow protons corresponding to the diffraction region were accepted, but pions were rejected. Therefore, the events *used* in the neutron detection efficiency study were restricted to those triggered by *recoil protons.*

The next consideration is: What fraction of these events were elastic and what fraction were inelastic? If there were many inelastic events with the $\bar{A}_1\bar{A}_2P_1P_2$ trigger, then when the neutrons converted in the neutron chambers (which happened more than half the time) we would see a proton-neutron event which did *not* fit the elastic criteria. However, in 85% of the events triggered by $\bar{A}_1\bar{A}_2P_1P_2$, in which a neutron converted in the neutron chamber, the event fitted the elastic criteria. Now the neutron chambers are very large compared to the spread in the predicted position of the neutron from an elastic event. Furthermore, we can deduce from the distribution of inelastic neutron events that the fraction of events is small which are inelastic and whose neutron passes outside the neutron chambers. Therefore, the events whose trigger is $\bar{A}_1\bar{A}_2P_1P_2$ and do not show neutrons in the neutron chamber, are overwhelmingly elastic events whose neutrons do not convert, rather than inelastic events whose neutrons pass outside the neutron chambers.

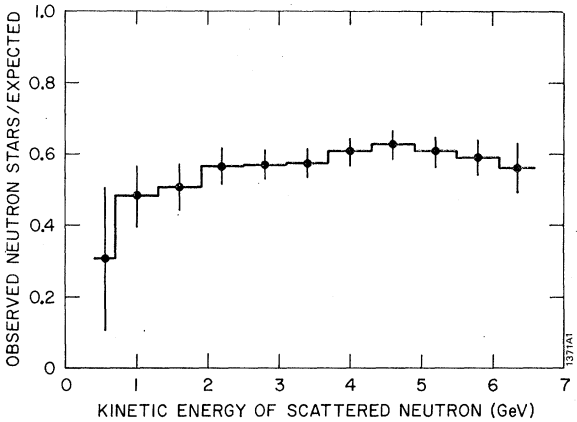

FIG. 8. Neutron detection efficiency as a function of the kinetic energy of the scattered neutron.

Figure 8 shows the ratio of observed interactions to the total number expected versus the kinetic energy of the scattered neutron. This ratio represents the product of the efficiency of the chambers to "convert" neutrons to charged particles, and of the efficiency of the scanners to identify the interactions. At the higher neutron energies, the ratio is roughly flat and is approximately 55–60%, which is consistent with the total number of collision lengths represented by the chambers.

B. Weighting Function

Because of the length of the target and the solid-angle acceptance of the neutron and proton arms, the probability at a given setting of the arms for observing an elastic scattering involving a particular four-momentum transfer $|t|_i$ is a function of the incident neutron energy and the point of interaction in the target. This probability was calculated using Monte Carlo methods, and when cross sections were calculated, every elastic event was weighted according to this probability. The cross sections presented in this paper differ from those in Refs. 1–4 as an error was discovered in the manner in which the phi acceptance of the apparatus was treated. In addition, we have used some recent data on the real part of the scattering amplitude in calculating the cross section at $t=0$.

C. Target Empty

The contamination of the elastic sample from interactions that did not take place in the hydrogen was

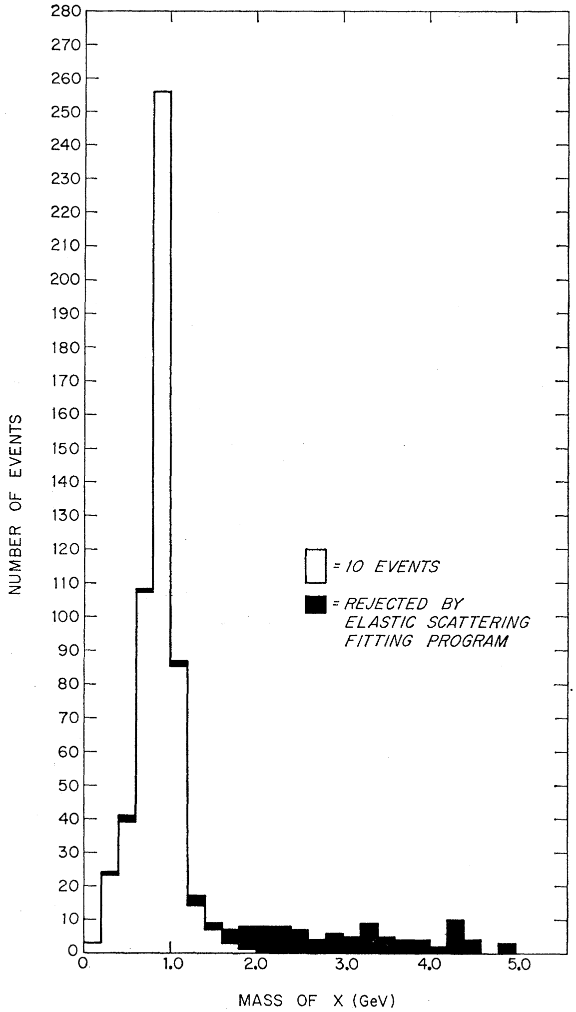

FIG. 9. Distribution of the mass of the X particle when the scatterings are interpreted as $X+P \rightarrow X+P$. A large peak at the neutron mass is observed. Events rejected by the fitting program are indicated.

found by taking a number of pictures under normal triggering conditions but with the target empty. Because of the care taken with the construction of the target vessel, the number of "fake" elastic events appearing to come from the fiducial volume, and, hence, the target-empty correction was negligible.

D. Beam Contamination

Because every elastic event was overdetermined, it was possible to test for the presence in the beam of contamination from particles other than neutrons which could fake np scattering. The method was to consider each event to be

$$X+p \rightarrow X+p\,, \qquad (24)$$

where the mass of the X particle is unknown. The distribution of the mass of X for all measured frames shows a large peak at the neutron mass value and a fairly uniform background, presumably from inelastic events which shift the mass of the neutron when the reaction

$$n+p \rightarrow n+p+k\pi \quad (k=1,2,\ldots) \qquad (25)$$

is interpreted as the two-body reaction; i.e., Eq. (24). When one removed those events rejected by the elastic scattering fitting program, a clean neutron peak remains. Figure 9 shows the results of the calculations for a small portion of the data. The same kind of result was also obtained when the events were interpreted as

$$n+p \rightarrow p+X\,. \qquad (26)$$

Again, the neutron peak is quite prominent, indicating that there were no very large contaminations present. The only possible contaminants are K^0's and γ rays. The K^0/neutron ratio above 1 GeV/c is $<1\%$. The cross section for large-angle γ scattering on hydrogen is extremely small, and, therefore, the effects of any contaminants are expected to be negligible.

E. χ^2 Distribution

A more sensitive test for inelastic contaminations involves the distribution of χ^2. The distribution of χ^2 for a set of measurements subjected to a two-constraint fit is known to fall off steeply for large values χ^2. As mentioned before, if this set of measurements contains no background, then less than 2% of the measurements will have χ^2 greater than 8.0. Thus, the distribution of χ^2 for large χ^2 is primarily due to the presence of background. It can be shown that when this background is randomly distributed, a two-constraint fit produces a flat distribution of χ^2 for this background.

A flat background was, therefore, assumed, and an estimate was made of it based on the number of events with χ^2 between 19 and 50. This calculation was done for small $|t|$ intervals over the entire angular and incident momentum range covered by the experiment. It was found that the inelastic contamination was less than 1% at the smallest $|t|$ and $33\%\pm25\%$ in the worst case. Corrections for these backgrounds were made.

VI. PRESENTATION OF DATA

A. Neutron Spectrum

The shape of the energy distribution of the incident neutron beam shown in Fig. 10 was obtained from the number of elastic events versus energy after unfolding the neutron detection efficiency and the cross section. The spectrum is seen to peak at high energies with the maximum around 5.0 GeV and with two-thirds of the observed neutrons having kinetic energies greater than 4.0 GeV. This high-energy spectrum was, in fact, a more favorable one than had been anticipated. The neutron intensity, with the collimator system subtending approximately 3.87×10^{-6} sr at 1° with respect to the external proton beam, was roughly 1.5×10^{5} neutrons

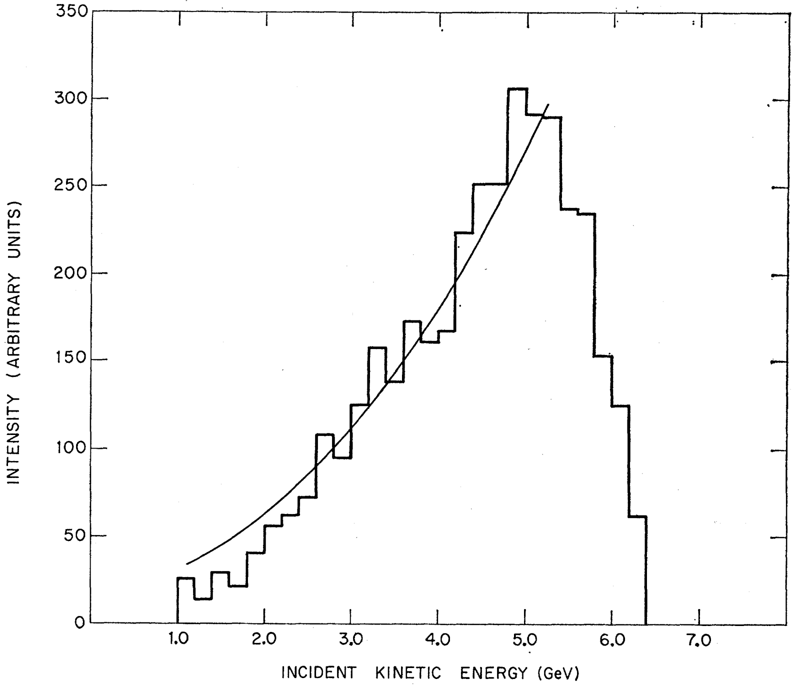

FIG. 10. Energy spectrum of the neutron beam. The curve is an expression obtained for inelastic proton production [Eq. (27)].

(in the energy range from 1 to 6.3 GeV) for 10^{10} protons in the external beam.

It is interesting to see if this spectrum is consistent with production data for other elementary particles, in particular for proton production. Trilling has examined the data for inelastic production of protons from beryllium[27] and has summarized the information in an empirical fit valid for a large range of energies. The formuls giving the number of protons of momentum p into a solid angle $d\Omega=\sin\theta d\theta d\varphi$ is

$$\frac{d^2N}{dp d\Omega}=p^2\left(1+0.47\frac{P_B}{p^2}\right)\times\left[\frac{0.56}{P_B}+\frac{0.44}{P_B{}^2}p\left(1-\frac{0.47P_B}{p^2}\right)\right]e^{-3.0(p\theta)^2}, \quad (27)$$

where P_B is the momentum of the incident beam. If the production of inelastic nucleons is relatively independent of charge for small θ and large P_B, this formula may be applied to the neutron spectrum. It is reasonable to expect approximate charge independence, because in a nucleon-nucleon collision accompanied by the emission of more than one pion, the inelastically produced nucleon is as likely to be a neutron as a proton. Also, because the production target is low Z, one does not expect nuclear effects to be important. As shown in Fig. 10, Eq. (27) appears to agree well with the observed spectrum for energies up to about 5.5 GeV. Above 5.5 GeV the spectrum falls off rapidly to the maximum energy, determined by the energy of the proton beam. The total yield of neutrons is also in reasonable agreement with Eq. (27).

B. Normalizations

There are two questions of normalization involved in the presentation of the differential cross sections—relative and absolute.

As mentioned before, four sets of counter telescopes were used to monitor the incident beam, the G, H, B, and M telescopes (see Fig. 4). Since the rates in these counters are proportional to the incident neutron flux, they were used to provide the relative normalization between settings. Unfortunately, it was not possible to use the B and M counters for all settings. Approximately halfway through the run, movement of a large shielding block caused the position of the B counters to shift slightly, changing the counting rate. The M counters were not used, for when the magnet system was positioned to measure recoil protons with small lab angles part of the magnet and its support carriage blocked the M counters. None of these troubles affected the G and H counting rates, which were found to be reproducible within statistics.

Another method was used to check this normalization. The regions of the differential cross section measured by successive settings overlapped. Comparison of the cross sections in the overlap region measured at the two settings serves as a consistency check of the normalization. This method agrees with the normalizations attained from the G and H counters within the statistics.

---

[2] *200-BeV Accelerator Design Study* (Lawrence Radiation Laboratory, University of California, Berkeley, 1965), Vol. 1, Sec. XIII 1.3, p. XIII-6.

The experiment itself did not allow a measurement of the absolute cross sections. However, these were obtained as follows. The differential cross section can be written as

$$(d\sigma/d\Omega)(\theta)=[\mathrm{Re}f(\theta)]^2+[\mathrm{Im}f(\theta)]^2. \qquad (28)$$

Using the optical theorem this becomes, for $\theta=0$,

$$(d\sigma/d\Omega)(0°)=(4\pi/p^*)\sigma_T{}^2(1+\rho_n{}^2), \qquad (29)$$

where

$$\rho_n=\mathrm{Re}f(0°)/\mathrm{Im}f(0°). \qquad (30)$$

Here σ_T is the total cross section and p^* is the neutron momentum in the barycentric systems. Equation (29) indicates that the absolute values of the differential cross section at 0° depend upon total cross-section measurements and on the value of ρ_n.

In order to apply the optical theorem to normalize the scattering cross sections, it is necessary to make some assumptions regarding the behavior of the helicity amplitudes. These assumptions, commonly made at high energies, are discussed below.

At 0°, angular momentum conservation allows only three helicity amplitudes, in each isotopic spin state, to be nonzero for either proton-proton or neutron-proton elastic scattering. These amplitudes are $F_{++,++}{}^I$, $F_{+-,+-}{}^I$, and $F_{++,--}{}^I$ where $I=0$ or 1. At 0°, Eqs. (5) and (6) therefore reduce to

$$(d\sigma/d\Omega)^{pp}(0°)=\tfrac{1}{2}|F_{++,++}{}^1(0°)|^2 +\tfrac{1}{2}|F_{--,++}{}^1(0°)|^2+\tfrac{1}{2}|F_{+-,+-}{}^1(0°)|^2,$$

$$(d\sigma/d\Omega)^{np}(0°)=\tfrac{1}{8}|F_{++,++}{}^1(0°)+F_{++,++}{}^0(0°)|^2 +\tfrac{1}{8}|F_{+-,+-}{}^1(0°)+F_{+-,++}{}^0(0°)|^2 +\tfrac{1}{8}|F_{--,++}{}^1(0°)+F_{--,++}{}^0(0°)|^2.$$

However, the optical theorem relates the total cross section to the imaginary parts of only two of amplitudes $F_{++,++}{}^I$ and $F_{+-,+-}{}^I$ in each isotopic spin state at 0°.

At high energies, the following assumptions are made in both np and pp scattering experiments. It is assumed that the double helicity flip amplitudes $F_{--,++}{}^I$ are zero and that the remaining two amplitudes in each isotopic spin state have the same θ dependence near 0°. This is equivalent to the statement that for forward elastic scattering, spin does not play an important role and that there is only one spin-independent amplitude. Either this assumption, or the assumption that the two remaining amplitudes are equal, allows the use of the optical theorem [Eq. (29)] to calculate the 0° point on the differential cross section.

The real and imaginary parts of the np scattering amplitude were calculated from pd and pp experimental data in a manner consistent with these assumptions.

These assumptions are most suspect at low energies and are probably not valid below 1 GeV. The validity of these assumptions to normalize our data is evidenced by the fact that our cross sections, when extrapolated, seem to join the cross sections of Ref. 28 at 991 MeV.

Measurements of the total neutron-proton cross sections have been of two types: the direct method and the subtraction method. The few direct measurements[29,30] are transmission experiments using neutron beams. The data, which have quoted errors ranging from 4 to 10%, unfortunately, give the cross sections at only a few energies in the range of interest. The subtraction measurements,[31] however, cover the momentum interval from 2 to 8 GeV/c in great detail. The analysis involves the comparison of the total cross sections for proton-proton and proton-deuteron scattering. The pd total cross section can be expressed in terms of the pp and np total cross sections by the Glauber formula[31–34]

$$\sigma_t(pd)=\sigma_t(pp)+\sigma_t(np) -[\sigma_t(pp)\sigma_t(np)(1-\rho_n\rho_p)(\langle r^{-2}\rangle/4\pi)], \qquad (31)$$

where ρ_p and ρ_n are the ratios of the real part to the imaginary part of the scattering amplitude for pp and np scattering, respectively, and $\langle r^{-2}\rangle$ is a factor which may roughly be described as the mean square radius of the deuteron. The last factor in Eq. (31) is small and relatively insensitive to the actual value of ρ_n. However, the uncertainty in the choice of $\langle r^{-2}\rangle$ limits the accuracy of np total cross sections obtained from Eq. (31) to $\approx\pm5\%$.

An experimental determination of ρ_n can be made using Eq. (31) and a direct measurement of $\sigma_t(np)$,[35,36] or can be performed by using a formula equivalent to Eq. (31) which compares the small-angle pd and pp differential cross sections. The data[32] at momenta near 20 GeV/c indicate that ρ_n is approximately -0.33, while the data[37] in the range from 2 to 7 GeV/c are consistent with ρ_n being -0.45. Present data on ρ_n and calculations based on dispersion relations[38,39] agree at

---

[28] T. A. Murray, L. Riddiford, G. H. Grayer, T. W. Jones, and Y. Tanimura, Nuovo Cimento **49A**, 261 (1967); and T. A. Murray (private communication).

[29] H. Palevsky, J. L. Friedes, R. J. Sutter, R. E. Chrien, and R. H. Muether, in *C. R. Congrès International de Physique Nucléaire, 1964*, edited by Mme. P. Gugenberger (Editions du Centre National de la Recherche Scientifique, Paris, 1964), Vol. II, p. 162.

[30] V. S. Pantuev, M. N. Kachaturyan, and I. V. Chuvilo, Yadern. Fiz. **1**, 134 (1965) [English transl.: Soviet J. Nucl. Phys. **1**, 93 (1965)].

[31] D. V. Bugg, D. C. Salter, C. H. Stafford, R. F. George, K. F. Riley, and R. J. Tapper, Phys. Rev. **146**, 980 (1966).

[32] G. Bellettini, G. Cocconi, A. N. Diddens, E. Lillethun, G. Matthiae, J. P. Scanlon, and A. M. Wetherell, Phys. Letters **19**, 341 (1965).

[33] R. J. Glauber, Phys. Rev. **100**, 242 (1955).

[34] D. R. Harrington, Phys. Rev. **135**, B358 (1964).

[35] L. Kirillova, V. Nikitin, A. Nomofilov, V. Pantuev, M. Shafranova, I. Sitnik, L. Slepetz, L. Strunov, V. Sviridov, L. Zolin, M. Khachaturian, Z. Korbel, L. Rob, P. Devinski, L. Khristov, P. Markov, K. H. Tchernev, and Z. Zlatanov, abstract presented at Oxford International Conference on Elementary Particles, 1965; abstract No. JINR-E-2413, 1965 (unpublished).

[36] L. S. Zolin, L. F. Kirillova, Lu Ch'ing-ch'iang, V. A. Nikitin, V. S. Pantuev, V. A. Sviridov, L. N. Strunov, M. N. Khachaturyan, M. G. Shafranova, Z. Korbel, L. Rob. P. Devinski, Z. Zlatanov, P. Markov, L. Khristov, Kh. Chernev, N. Dalkhazhav, and D. Tuvdendorzh, Zh. Eksperim. i Teor. Fiz. Pis'ma v Redaktsiya **3**, 15 (1956) [English transl.: JETP Letters **3**, 8 (1966)].

[37] N. Kalkhazhav *et al.*, Yadern. Fiz. **8**, 342 (1969) [English transl.: Soviet J. Nucl. Phys. **8**, 196 (1969)].

[38] P. Söding, Phys. Letters **8**, 285 (1964).

[39] A. A. Carter and D. V. Bugg, Phys. Letters **20**, 203 (1966).

TABLE I. Neutron-proton elastic scattering differential cross sections. $\cos\theta$ and $(d\sigma/d\Omega)$ are in the barycentric system. θ is the angle corresponding to the central $|t|$ value and central incident neutron momentum. The differential cross sections are all normalized using the optical theorem (with the total cross sections of Ref. 31) and taking the ratio of the real part to the imaginary part of the *np* forward scattering amplitude to be −0.45.

$\|t\|$ range $(\mathrm{GeV}/c)^2$	$\|t\|$ central $(\mathrm{GeV}/c)^2$	$\frac{d\sigma}{d\|t\|}$ [mb/(GeV/*c*)²]	$\cos\theta$	$\frac{d\sigma}{d\Omega}$ (mb/sr)	Events
Incident neutron momentum 1.70–2.25 GeV/*c* Kinetic energy 1.00–1.50 GeV (1132 events)				Central value = 1.97 GeV/*c*	
		105.53[a]			
0.10–0.20	0.150	46.008 ±5.237	0.872	8.594 ±0.978	153
0.20–0.30	0.250	23.956 ±3.038	0.787	4.475 ±0.567	89
0.30–0.40	0.350	15.326 ±1.744	0.702	2.863 ±0.326	149
0.40–0.50	0.450	8.090 ±1.037	0.617	1.511 ±0.194	100
0.50–0.60	0.550	7.501 ±0.918	0.531	1.401 ±0.171	127
0.60–0.70	0.650	3.336 ±0.442	0.446	0.623 ±0.083	85
0.70–0.80	0.750	2.722 ±0.457	0.361	0.508 ±0.085	56
0.80–0.90	0.850	1.957 ±0.297	0.276	0.366 ±0.056	64
0.90–1.00	0.950	1.536 ±0.260	0.191	0.287 ±0.049	59
1.00–1.25	1.125	1.034 ±0.176	0.041	0.193 ±0.033	106
1.25–1.55	1.400	1.077 ±0.224	−0.193	0.201 ±0.042	144
Incident neutron momentum 2.25–2.79 GeV/*c* Kinetic energy 1.50–2.00 GeV (1420 events)				Central value = 2.51 GeV/*c*	
		112.70[a]			
0.10–0.20	0.150	49.933 ±5.295	0.909	13.058 ±1.385	189
0.20–0.30	0.250	19.447 ±2.073	0.848	5.085 ±0.542	137
0.30–0.40	0.350	13.582 ±1.681	0.787	3.552 ±0.439	104
0.40–0.50	0.450	7.128 ±0.761	0.726	1.864 ±0.199	132
0.50–0.60	0.550	3.745 ±0.468	0.665	0.979 ±0.122	81
0.60–0.70	0.650	2.397 ±0.382	0.604	0.627 ±0.099	44
0.70–0.80	0.750	1.706 ±0.223	0.544	0.446 ±0.058	72
0.80–0.90	0.850	1.090 ±0.154	0.483	0.285 ±0.040	59
0.90–1.00	0.950	1.051 ±0.153	0.422	0.275 ±0.040	54
1.00–1.20	1.100	0.636 ±0.084	0.331	0.166 ±0.022	79
1.20–1.40	1.300	0.506 ±0.064	0.209	0.132 ±0.017	100
1.40–1.60	1.500	0.353 ±0.049	0.087	0.092 ±0.013	74
1.60–1.80	1.700	0.270 ±0.041	−0.035	0.071 ±0.011	67
1.80–2.00	1.900	0.299 ±0.049	−0.156	0.078 ±0.013	71
2.00–2.49	2.245	0.391 ±0.080	−0.366	0.102 ±0.021	157
Incident neutron momentum 2.79–3.31 GeV/*c* Kinetic energy 2.00–2.50 GeV (1558 events)				Central value = 3.05 GeV/*c*	
		114.08[a]			
0.10–0.20	0.150	44.437 ±4.030	0.929	14.941 ±1.355	202
0.20–0.30	0.250	18.111 ±1.553	0.882	6.089 ±0.522	195
0.30–0.40	0.350	8.262 ±1.003	0.834	2.778 ±0.337	79
0.40–0.50	0.450	6.267 ±0.782	0.787	2.107 ±0.263	91
0.50–0.60	0.550	3.663 ±0.391	0.740	1.231 ±0.132	102
0.60–0.70	0.650	1.927 ±0.268	0.692	0.648 ±0.090	57
0.70–0.80	0.750	1.535 ±0.259	0.645	0.516 ±0.087	38
0.80–0.90	0.850	1.223 ±0.171	0.598	0.411 ±0.058	63
0.90–1.00	0.950	0.666 ±0.103	0.550	0.224 ±0.035	47
1.00–1.20	1.100	0.714 ±0.083	0.479	0.240 ±0.028	104
1.20–1.40	1.300	0.597 ±0.075	0.385	0.201 ±0.025	86
1.40–1.60	1.500	0.337 ±0.040	0.290	0.113 ±0.014	90
1.60–1.80	1.700	0.277 ±0.035	0.195	0.093 ±0.012	77
1.80–2.20	2.000	0.171 ±0.020	0.053	0.057 ±0.007	109
2.20–2.60	2.400	0.115 ±0.015	−0.136	0.039 ±0.005	94
2.60–3.00	2.800	0.140 ±0.025	−0.325	0.047 ±0.008	80
3.00–3.43	3.215	0.122 ±0.031	−0.522	0.041 ±0.010	44
Incident neutron momentum 3.31–3.83 GeV/*c* Kinetic energy 2.50–3.00 GeV (1514 events)				Central value = 3.57 GeV/*c*	
		111.20[a]			
0.10–0.20	0.150	43.885 ±3.679	0.942	18.034 ±1.512	226
0.20–0.30	0.250	15.932 ±1.214	0.903	6.547 ±0.499	220
0.30–0.40	0.350	8.703 ±0.860	0.864	3.577 ±0.353	117
0.40–0.50	0.450	5.564 ±0.729	0.826	2.286 ±0.300	73
0.50–0.60	0.550	3.327 ±0.356	0.787	1.367 ±0.146	99
0.60–0.70	0.650	1.432 ±0.188	0.748	0.588 ±0.077	63
0.70–0.80	0.750	0.808 ±0.143	0.710	0.332 ±0.059	34
0.80–0.90	0.850	0.687 ±0.142	0.671	0.282 ±0.058	25
0.90–1.00	0.950	0.654 ±0.096	0.632	0.269 ±0.040	52
1.00–1.20	1.100	0.442 ±0.050	0.574	0.182 ±0.021	96
1.20–1.40	1.300	0.232 ±0.035	0.497	0.096 ±0.014	49

TABLE I (*continued*)

$\lvert t\rvert$ range (GeV/c)^2	$\lvert t\rvert$ central (GeV/c)^2	$\frac{d\sigma}{d\lvert t\rvert}$ [mb/(GeV/c)^2]	$\cos\theta$	$\frac{d\sigma}{d\Omega}$ (mb/sr)	Events
1.40–1.60	1.500	0.218 ±0.033	0.419	0.090 ±0.014	50
1.60–1.80	1.700	0.164 ±0.022	0.342	0.067 ±0.010	61
1.80–2.00	1.900	0.130 ±0.019	0.264	0.053 ±0.008	53
2.00–2.50	2.250	0.084 ±0.012	0.129	0.035 ±0.005	65
2.50–3.00	2.750	0.081 ±0.009	−0.065	0.033 ±0.004	113
3.00–3.50	3.250	0.045 ±0.007	−0.259	0.018 ±0.003	56
3.50–4.37	3.935	0.059 ±0.012	−0.524	0.024 ±0.005	62
Incident neutron momentum 3.83–4.34 GeV/c Kinetic energy 3.00–3.50 GeV (1492 events)				Central value = 4.08 GeV/c	
		110.70[a]			
0.10–0.20	0.150	36.458 ±2.676	0.951	17.706 ±1.300	251
0.20–0.30	0.250	18.225 ±1.196	0.918	8.851 ±0.581	295
0.30–0.40	0.350	8.090 ±0.708	0.885	3.929 ±0.344	150
0.40–0.50	0.450	4.257 ±0.559	0.853	2.067 ±0.272	63
0.50–0.60	0.550	2.473 ±0.337	0.820	1.201 ±0.164	73
0.60–0.70	0.650	1.559 ±0.192	0.787	0.757 ±0.093	75
0.70–0.80	0.750	1.007 ±0.141	0.754	0.489 ±0.068	57
0.80–0.90	0.850	0.413 ±0.090	0.721	0.200 ±0.044	22
0.90–1.00	0.950	0.612 ±0.119	0.689	0.297 ±0.058	28
1.00–1.20	1.100	0.256 ±0.034	0.640	0.125 ±0.017	61
1.20–1.40	1.300	0.227 ±0.030	0.574	0.110 ±0.014	62
1.40–1.60	1.500	0.171 ±0.028	0.508	0.083 ±0.013	41
1.60–1.80	1.700	0.109 ±0.018	0.443	0.053 ±0.009	40
1.80–2.00	1.900	0.072 ±0.013	0.377	0.035 ±0.006	35
2.00–2.50	2.250	0.050 ±0.007	0.263	0.024 ±0.003	62
2.50–3.00	2.750	0.037 ±0.007	0.099	0.018 ±0.003	33
3.00–3.50	3.250	0.026 ±0.004	−0.065	0.013 ±0.002	39
3.50–4.00	3.750	0.023 ±0.004	−0.229	0.011 ±0.002	35
4.00–4.50	4.250	0.019 ±0.004	−0.393	0.009 ±0.002	33
4.50–5.30	4.900	0.055 ±0.013	−0.606	0.027 ±0.006	37
Incident neutron momentum 4.34–4.85 GeV/c Kinetic energy 3.50–4.00 GeV (1608 events)				Central value = 4.59 GeV/c	
		109.63[a]			
0.10–0.20	0.150	34.847 ±2.177	0.957	19.527 ±1.220	357
0.20–0.30	0.250	11.930 ±0.770	0.929	6.685 ±0.431	319
0.30–0.40	0.350	6.294 ±0.490	0.901	3.527 ±0.275	205
0.40–0.50	0.450	3.037 ±0.354	0.872	1.702 ±0.199	84
0.50–0.60	0.550	1.484 ±0.217	0.844	0.832 ±0.122	62
0.60–0.70	0.650	0.973 ±0.121	0.815	0.545 ±0.068	73
0.70–0.80	0.750	0.573 ±0.080	0.787	0.321 ±0.045	56
0.80–0.90	0.850	0.414 ±0.068	0.759	0.232 ±0.038	39
0.90–1.00	0.950	0.248 ±0.055	0.730	0.139 ±0.031	21
1.00–1.20	1.100	0.210 ±0.031	0.688	0.118 ±0.017	60
1.20–1.40	1.300	0.117 ±0.016	0.631	0.065 ±0.009	57
1.40–1.60	1.500	0.078 ±0.013	0.574	0.044 ±0.007	37
1.60–1.80	1.700	0.055 ±0.012	0.517	0.031 ±0.007	22
1.80–2.00	1.900	0.025 ±0.006	0.460	0.014 ±0.003	21
2.00–2.50	2.250	0.021 ±0.003	0.361	0.012 ±0.002	47
2.50–3.00	2.750	0.014 ±0.003	0.219	0.008 ±0.002	23
3.00–3.50	3.250	0.011 ±0.003	0.077	0.006 ±0.001	17
3.50–4.00	3.750	0.009 ±0.002	−0.065	0.005 ±0.001	15
4.00–4.50	4.250	0.012 ±0.002	−0.207	0.007 ±0.001	31
4.50–5.00	4.750	0.012 ±0.002	−0.349	0.007 ±0.001	35
5.00–5.50	5.250	0.005 ±0.002	−0.491	0.003 ±0.001	6
5.50–6.25	5.875	0.020 ±0.006	−0.669	0.011 ±0.003	21
Incident neutron momentum 4.85–5.36 GeV/c Kinetic energy 4.00–4.50 GeV (1708 events)				Central value = 5.10 GeV/c	
		108.67[a]			
0.11–0.20	0.155	33.477 ±2.080	0.961	21.261 ±1.321	346
0.20–0.30	0.250	16.948 ±1.000	0.937	10.763 ±0.635	420
0.30–0.40	0.350	7.206 ±0.523	0.912	4.576 ±0.332	254
0.40–0.50	0.450	3.464 ±0.369	0.887	2.200 ±0.234	106
0.50–0.60	0.550	1.903 ±0.264	0.862	1.208 ±0.168	66
0.60–0.70	0.650	1.036 ±0.134	0.837	0.658 ±0.085	69
0.70–0.80	0.750	0.545 ±0.075	0.812	0.346 ±0.048	56
0.80–0.90	0.850	0.568 ±0.079	0.787	0.360 ±0.050	55
0.90–1.00	0.950	0.281 ±0.055	0.762	0.179 ±0.035	27
1.00–1.20	1.100	0.197 ±0.035	0.724	0.125 ±0.022	34
1.20–1.40	1.300	0.090 ±0.014	0.674	0.057 ±0.009	43

TABLE I (*continued*)

$\|t\|$ range (GeV/c)^2	$\|t\|$ central (GeV/c)^2	$\frac{d\sigma}{d\|t\|}$ [mb/(GeV/c)^2]	cosθ	$\frac{d\sigma}{d\Omega}$ (mb/sr)	Events
1.40–1.60	1.500	0.060 ±0.011	0.624	0.038 ±0.007	32
1.60–1.80	1.700	0.044 ±0.010	0.574	0.028 ±0.006	21
1.80–2.00	1.900	0.028 ±0.009	0.524	0.018 ±0.005	11
2.00–2.50	2.250	0.014 ±0.002	0.436	0.009 ±0.002	33
2.50–3.00	2.750	0.016 ±0.003	0.311	0.010 ±0.002	32
3.00–3.50	3.250	0.010 ±0.002	0.186	0.006 ±0.002	16
3.50–4.18	3.840	0.004 ±0.001	0.038	0.003 ±0.001	10
4.33–5.00	4.665	0.006 ±0.002	−0.169	0.004 ±0.001	16
5.00–5.50	5.250	0.006 ±0.002	−0.316	0.004 ±0.001	19
5.50–6.00	5.750	0.010 ±0.003	−0.441	0.006 ±0.002	15
6.00–6.50	6.250	0.012 ±0.003	−0.566	0.008 ±0.002	13
6.50–7.18	6.840	0.017 ±0.005	−0.714	0.010 ±0.003	14
Incident neutron momentum 5.36–5.87 GeV/c Kinetic energy 4.50–5.00 GeV (1943 events)				Central value = 5.61 GeV/c	
		108.06^{a}			
0.11–0.20	0.155	39.129 ±2.611	0.965	27.774 ±1.853	386
0.20–0.30	0.250	17.365 ±1.161	0.944	12.326 ±0.824	420
0.30–0.40	0.350	8.532 ±0.583	0.922	6.056 ±0.414	332
0.40–0.50	0.450	4.792 ±0.413	0.899	3.402 ±0.293	170
0.50–0.60	0.550	2.231 ±0.302	0.877	1.584 ±0.214	59
0.60–0.70	0.650	1.480 ±0.150	0.854	1.051 ±0.106	110
0.70–0.80	0.750	0.791 ±0.091	0.832	0.562 ±0.065	81
0.80–0.90	0.850	0.455 ±0.066	0.809	0.323 ±0.047	51
0.90–1.00	0.950	0.305 ±0.056	0.787	0.217 ±0.040	31
1.00–1.20	1.100	0.167 ±0.030	0.753	0.118 ±0.021	32
1.20–1.40	1.300	0.158 ±0.024	0.709	0.112 ±0.017	56
1.40–1.60	1.500	0.055 ±0.010	0.664	0.039 ±0.007	35
1.60–1.80	1.700	0.030 ±0.007	0.619	0.022 ±0.005	18
1.80–2.00	1.900	0.027 ±0.008	0.574	0.019 ±0.006	12
2.00–2.50	2.250	0.022 ±0.004	0.495	0.015 ±0.003	36
2.50–3.00	2.750	0.013 ±0.002	0.383	0.009 ±0.002	33
3.00–3.50	3.250	0.004 ±0.002	0.271	0.003 ±0.001	7
3.50–4.48	3.990	0.004 ±0.001	0.105	0.003 ±0.001	13
4.99–6.00	5.495	0.004 ±0.001	−0.232	0.003 ±0.001	21
6.00–6.50	6.250	0.005 ±0.002	−0.401	0.003 ±0.001	9
6.50–7.00	6.750	0.006 ±0.002	−0.514	0.004 ±0.001	9
7.00–7.50	7.250	0.013 ±0.004	−0.626	0.009 ±0.003	15
7.50–7.97	7.735	0.012 ±0.005	−0.734	0.008 ±0.003	7
Incident neutron momentum 5.87–6.37 GeV/c Kinetic energy 5.00–5.50 GeV (1809 events)				Central value = 6.12 GeV/c	
		107.38^{a}			
0.13–0.20	0.165	30.350 ±2.318	0.967	23.810 ±1.818	298
0.20–0.30	0.250	15.191 ±0.970	0.949	11.918 ±0.761	471
0.30–0.40	0.350	6.116 ±0.421	0.929	4.798 ±0.330	318
0.40–0.50	0.450	3.240 ±0.283	0.909	2.542 ±0.222	158
0.50–0.60	0.550	2.269 ±0.267	0.888	1.780 ±0.209	79
0.60–0.70	0.650	1.196 ±0.118	0.868	0.938 ±0.093	114
0.70–0.80	0.750	0.631 ±0.078	0.848	0.495 ±0.061	72
0.80–0.90	0.850	0.361 ±0.050	0.828	0.283 ±0.039	55
0.90–1.00	0.950	0.168 ±0.034	0.807	0.132 ±0.027	25
1.00–1.20	1.100	0.111 ±0.022	0.777	0.087 ±0.017	27
1.20–1.40	1.300	0.063 ±0.016	0.736	0.049 ±0.013	17
1.40–1.60	1.500	0.030 ±0.007	0.696	0.024 ±0.005	22
1.60–1.80	1.700	0.022 ±0.005	0.655	0.017 ±0.004	18
1.80–2.00	1.900	0.021 ±0.006	0.615	0.016 ±0.005	13
2.00–2.50	2.250	0.012 ±0.003	0.544	0.010 ±0.002	18
2.50–3.00	2.750	0.0059±0.0013	0.442	0.0046±0.0010	22
3.00–3.50	3.250	0.0047±0.0013	0.341	0.0037±0.0010	14
3.50–4.00	3.750	0.0058±0.0017	0.239	0.0046±0.0013	12
4.00–4.79	4.395	0.0012±0.0006	0.108	0.0010±0.0004	5
5.65–7.00	6.325	0.0022±0.0007	−0.283	0.0017±0.0005	14
7.00–8.00	7.500	0.0054±0.0013	−0.522	0.0042±0.0010	19
8.00–8.73	8.365	0.0116±0.0034	−0.697	0.0091±0.0027	18
Incident neutron momentum 6.37–7.18 GeV/c Kinetic energy 5.50–6.30 GeV (1482 events)				Central value = 6.77 GeV/c	
		106.71^{a}			
0.17–0.20	0.185	32.876 ±3.598	0.967	28.985 ±3.172	108
0.20–0.30	0.250	15.413 ±1.066	0.955	13.589 ±0.940	371
0.30–0.40	0.350	8.736 ±0.578	0.937	7.702 ±0.510	348

TABLE I (*continued*)

$\|t\|$ range (GeV/c)^2	$\|t\|$ central (GeV/c)^2	$\frac{d\sigma}{d\|t\|}$ [mb/(GeV/c)^2]	$\cos\theta$	$\frac{d\sigma}{d\Omega}$ (mb/sr)	Events
0.40–0.50	0.450	3.901 ±0.327	0.919	3.440 ±0.289	172
0.50–0.60	0.550	2.050 ±0.252	0.901	1.807 ±0.222	75
0.60–0.70	0.650	1.177 ±0.149	0.883	1.038 ±0.131	82
0.70–0.80	0.750	0.709 ±0.089	0.865	0.625 ±0.079	69
0.80–0.90	0.850	0.382 ±0.057	0.847	0.337 ±0.050	49
0.90–1.00	0.950	0.282 ±0.049	0.829	0.249 ±0.043	35
1.00–1.20	1.100	0.146 ±0.026	0.801	0.128 ±0.023	34
1.20–1.40	1.300	0.059 ±0.017	0.765	0.052 ±0.015	13
1.40–1.60	1.500	0.027 ±0.011	0.729	0.024 ±0.010	7
1.60–1.80	1.700	0.041 ±0.009	0.693	0.036 ±0.008	23
1.80–2.00	1.900	0.018 ±0.005	0.657	0.016 ±0.004	12
2.00–2.50	2.250	0.018 ±0.004	0.594	0.016 ±0.003	23
2.50–3.00	2.750	0.0057±0.0019	0.504	0.0050±0.0016	10
3.00–3.50	3.250	0.0036±0.0012	0.413	0.0032±0.0011	9
3.50–4.00	3.750	0.0047±0.0015	0.323	0.0041±0.0013	10
4.00–5.09	4.545	0.0011±0.0005	0.180	0.0010±0.0004	5
6.36–7.25	6.805	0.0034±0.0013	−0.228	0.0030±0.0011	8
7.35–8.50	7.925	0.0012±0.0006	−0.431	0.0011±0.0005	5
8.50–9.63	9.065	0.0056±0.0017	−0.636	0.0050±0.0015	14

[a] Differential cross section at $t=0$ by the optical theorem.

very high momenta and are in reasonable agreement in the 2–7-GeV/c region. For these reasons the cross sections were normalized with the assumption that $\rho_n = -0.45$.

Because the incident beam contained neutrons of all energies, the differential cross sections are presented for incident energy intervals, all but one of which are ½ GeV wide. Therefore, the calculations of the 0° cross sections for a given energy interval had to take the energy spectrum in the interval into consideration. The value at 0° was a weighted average of the 0° values for all energies in an interval, each value weighted according to the intensity of the observed neutron spectrum at that energy. The cross sections were then normalized by fitting the small-angle region with an exponential in $|t|$, extrapolating to 0°, and normalizing the 0° values to those given in Table I.

TABLE II. Values of B from the equation $(d\sigma/dt)=Ae^{B|t|}$ fitted to the given $|t|$ range of the differential cross section. The values are those quoted in the reference, if given, or are computed from the cross sections.

	Range of incident nucleon momenta (GeV/c)	Range of incident nucleon energy (GeV)	B (GeV/c)$^{-2}$	t range (GeV/c)^2	Ref.
pn (quasi-elastic)	1.68	0.991	−6.91±0.25	0.03–0.33	(28)
np	1.7– 2.3	1.0– 1.5	−5.66±0.54(−5.50±0.80)	0.1–0.5(0.1–0.4)	This expt.
	2.3– 2.8	1.5– 2.0	−6.22±0.48(−6.67±0.81)	0.1–0.5(0.1–0.4)	This expt.
	2.8– 3.3	2.0– 2.5	−6.86±0.48(−8.48±0.74)	0.1–0.5(0.1–0.4)	This expt.
	3.3– 3.8	2.5– 3.0	−7.14±0.46(−8.23±0.64)	0.1–0.5(0.1–0.4)	This expt.
	3.8– 4.3	3.0– 3.5	−7.33±0.43(−7.48±0.57)	0.1–0.5(0.1–0.4)	This expt.
	4.3– 4.8	3.5– 4.0	−8.25±0.38(−8.73±0.49)	0.1–0.5(0.1–0.4)	This expt.
	4.8– 5.4	4.0– 4.5	−7.65±0.36(−7.63±0.48)	0.1–0.5(0.1–0.4)	This expt.
	5.4– 5.9	4.5– 5.0	−7.11±0.33(−7.62±0.48)	0.1–0.5(0.1–0.4)	This expt.
	5.9– 6.4	5.0– 5.5	−7.94±0.37(−8.47±0.54)	0.1–0.5(0.1–0.4)	This expt.
	6.4– 7.2	5.5– 6.3	−7.31±0.44(−7.12±0.68)	0.1–0.5(0.1–0.4)	This expt.
	3.8– 6.9	3.0– 6.0	−6.9 ±1.0	0.006–0.3	46
	6.9–10.9	6.0–10.0	−8.6 ±0.9	0.006–0.3	46
	4.8– 6.9	4.0– 6.0	−6.2 ±0.3	0.3 –0.8	12
pp	1.68	0.991	−5.58±0.11	0.03 –0.33	28
	3.0	2.2	−6.50±0.04	0.01 –0.33	43
	5.0	4.1	−7.44±0.04	0.01 –0.33	43
	7.0	6.1	−7.69±0.03	0.01 –0.33	43
	6.8	5.9	−8.23±0.22	0.10 –0.40	44
	8.5	7.6	−7.75±0.11	0.13 –0.50	45
	8.8	7.9	−8.60±0.15	0.10 –0.42	44
	10.8	9.9	−8.69±0.17	0.12 –0.43	44

VII. RESULTS AND DISCUSSION

The differential cross sections ($d\sigma/dt$) are presented in Table I and in Fig. 11. The attached incident neutron laboratory momentum is the momentum at the center of the momentum interval, but the momentum limits of the interval are also given. The differential cross section is given as a function of $|t|$, with the corresponding value of $\cos\theta$ in the barycentric system also given. In the figures the solid line is drawn only to guide the eye. From these figures, the diffraction peak is seen to be approximately exponential at small $|t|$, but as $|t|$ approached 1 $(\mathrm{GeV}/c)^2$, the cross section begins to flatten out. This is typical of all high-energy hadron-hadron elastic scattering cross sections.

One of the purposes of this experiment was to look for deviations from smooth behavior of the cross section outside the small-$|t|$ region. In particular, it is interesting to look for structure in the region $|t|\approx 1$ $(\mathrm{GeV}/c)^2$ where dips and shoulders have been found for πp and

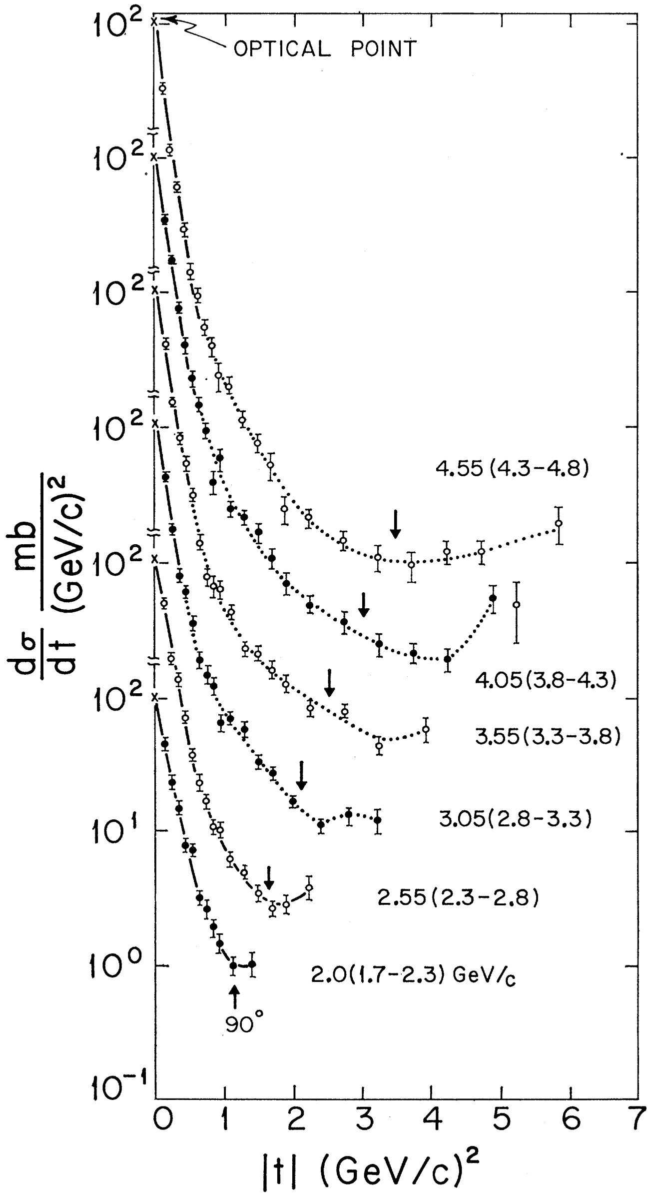

(a)

FIG. 11. Neutron-proton elastic scattering cross sections ($d\sigma/dt$) $[\mathrm{mb}/(\mathrm{GeV}/c)^2]$ versus $|t|$ $[(\mathrm{GeV}/c)^2]$ for the incident neutron momenta (GeV/c) indicated on each curve. The bracketed values are the range of the incident momenta and the preceding value is the central momentum. The solid lines are drawn only to guide the eye. The dotted curves are fits to the data explained in the text.

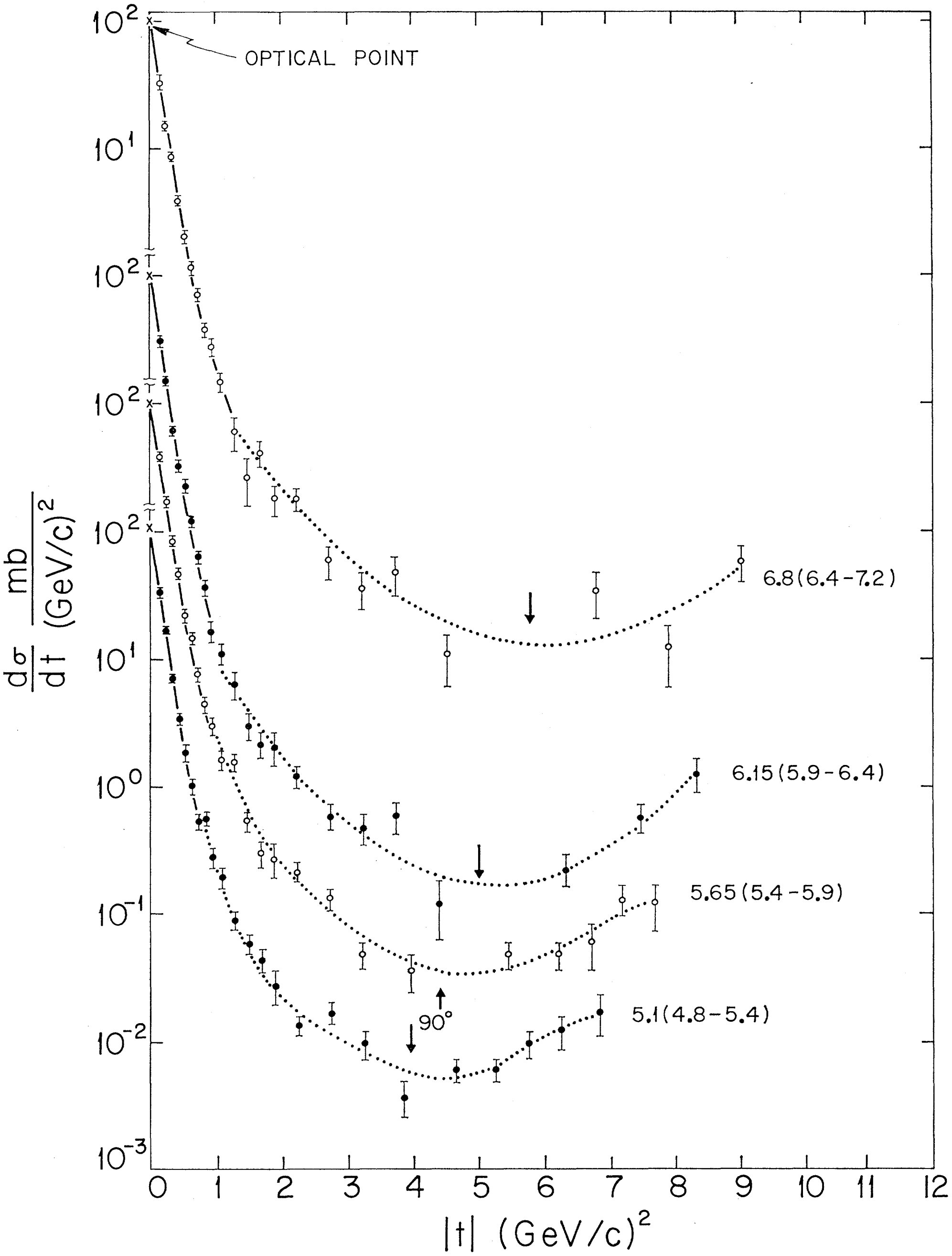

(b)

FIG. 11 (*continued*)

$\bar{p}p$ elastic scattering.[40–42] It is clear from Fig. 11 that our results show no marked structure. There is, however, the possibility of some structure, narrow in $|t|$ at the lower momenta. If this were so, the structure would have to be in the $I=0$ state, since no structure has been found in pp scattering at comparable momenta.[43] The data at large angles show several points which deviate

---

[40] D. E. Damouth, L. W. Jones, and M. L. Perl, Phys. Rev. Letters 11, 287 (1963).

[41] C. T. Coffin, N. Dikmen, L. Ettlinger, D. Meyer, A. Saulys, K. Terwilliger, and D. Williams, Phys. Rev. Letters 15, 838 (1965).

[42] B. Escoubes, A. Fedrighini, Y. Goldschmidt-Clermont, M. Guinea-Moorhead, T. Hofmokl, R. Lewisch, D. R. O. Morrison, M. Schneeberger, S. de Unamuno, H. C. Dehne, E. Lohrmann, E. Raubold, P. Söding, M. W. Teucher, and G. Wolf, Phys. Letters 5, 132 (1963).

[43] A. R. Clyde, Lawrence Radiation Laboratory, UCRL Report No. 16275, 1966 (unpublished).

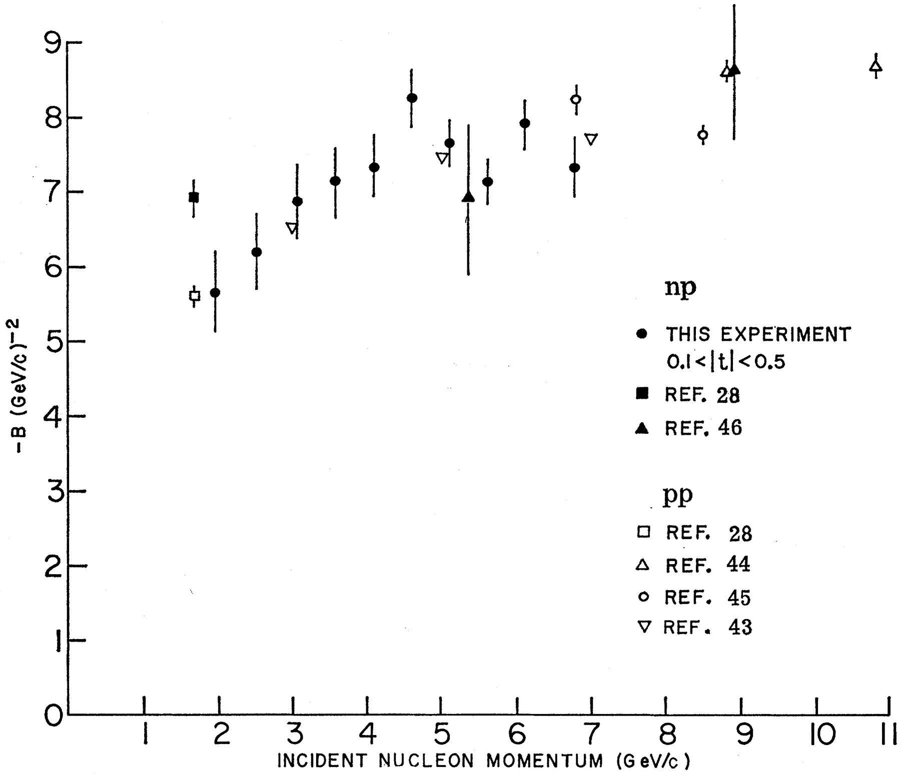

FIG. 12. Slopes of the diffraction peak [(GeV/*c*)$^{-2}$] for *np* (solid data points) and *pp* (open data points) elastic scattering versus the incident nucleon momenta (GeV/*c*).

significantly from the smooth curves. This could be due to systematic errors of an unknown nature that could also affect the data near $|t| \approx 1$ (GeV/*c*)^2. If these indications of structure were correct, it would be of considerable interest. Further measurements in the intermediate and large-angle region are clearly desirable.

In the diffraction region it has become customary to fit the differential cross section by the equation

$$d\sigma/dt = Ae^{B|t|}. \tag{32}$$

This equation was originally inspired by Regge theory but we can use it to compare *pp* and *np* diffraction scattering without any theoretical implications. Since the *np* data are absolutely normalized by using the optical theorem, the total *np* cross section and the real part of the *np* forward scattering cross section, A is not determined from our *np* data, and no comparison is made here. In Fig. 12 we compare the values of B for *pp*[43–45] and *np* scattering. In this figure we have also plotted a recent *np* bubble chamber measurement by Besliu *et al.*[46] We see that the *np* and *pp* exponential slopes B agree within the errors of the *np* points. Thus, even at these incident momenta the small-angle shape of the *pp* and *np* elastic cross sections is the same.

The near equality of the *pp* and *np* total cross sections, the relatively small differences between the known real parts of the *pp* elastic scattering amplitude and of the *np* elastic scattering amplitude means that the A parameter in Eq. (32) for the *pp* and *np* systems will be nearly the same. Therefore, in the diffraction region, *pp* and *np* have just about the same differential cross sections. From the optical-model point of view, the diffraction peak shape and size is a measure of the distribution of hadronic matter in the scattering system. Therefore, we can conclude that the distribution of hadronic matter in the neutron is very similar to that in the proton.

From the helicity-amplitude analysis of Eqs. (5) and (6), we see that we can assume that the corresponding $I=1$ and $I=0$ helicity amplitudes are equal for small θ. Remember that the corresponding amplitudes have opposite symmetries about 90°, so that as pointed out in Sec. II, this will mean a near cancellation of the amplitudes near 180°. Furthermore, if one neglects helicity flip, the simple model of Eq. (19) is adequate.

---

[44] K. J. Foley, S. J. Lindenbaum, W. A. Love, S. Ozaki, J. J. Russel, and L. C. L. Yuan, Phys. Rev. Letters **11**, 425 (1963). The values of B plotted in Fig. 2 were calculated from the cross sections for the $|t|$ values between 0.1 and 0.43 (GeV/*c*)^2 quoted in this reference.

[45] D. Harting, P. Blackall, B. Elsner, A. C. Helmholz, W. C. Middelkoop, B. Powell, B. Zacharov, P. Zanella, P. Dalpiaz, M. N. Focacci, S. Focardi, G. Giacomelli, L. Monari, J. A. Beaney, R. A. Donald, P. Mason, D. O. Caldwell, and L. W. Jones, Nuovo Cimento **38**, 60 (1965).

[46] C. Besliu, T. Besliu, A. Constantinescu, M. Gavrilas, A. Mihul, N. Gheordanescu, N. Hangea, M. Teleman, L. Teodorescu, I. Tipa, V. Karnauhov, V. Moroz, and L. Nefedeva, Nuovo Cimento **59A**, 1 (1969).

TABLE III. P_0 is the incident neutron momentum. The coefficients from the equation

$$\frac{d\sigma}{dt}=\exp\left(\sum_{n=0}^{k} a_n(\cos\theta)^n\right)$$

are least-squares fits to the differential cross section ($d\sigma/dt$) for $|\cos\theta|\leq 0.8$. k is the power of $\cos\theta$ yielding the greatest χ^2 probability. $F(\theta)$ is the ratio of the forward to backward differential cross section for the indicated value of $|\cos\theta|$. $\sigma_{90°}$ is the differential cross section at 90° c.m. $\cos\theta_{\min}$ is the $\cos\theta$ at which the differential cross section is smallest. w and w_t are measures of isotropy defined in the text.

P_0 (GeV/c)	k	Coefficients (0 to k)						$F(\cos\theta)$			From fit:			
		a_0	a_1	a_2	a_3	a_4	a_5	$\cos\theta=0.2$	$\cos\theta=0.4$	$\cos\theta=0.6$	$\sigma(90°)$ [mb/(GeV/c)^2]	$\cos\theta_{\min}$	w	w_t
3.0	5	−1.94	2.37	6.03	−8.07	−11.64	21.94	2.3±0.6	3.7±0.9	⋯	0.145 ±0.02	−0.2	⋯	⋯
3.6	4	−2.52	2.03	−0.475	−1.70	8.08	⋯	2.2±0.5	4.1±1.0	⋯	0.0795±0.013	−0.35	⋯	⋯
4.1	4	−3.54	2.14	1.28	−2.39	6.77	⋯	2.3±0.7	4.1±1.3	4.7±1.5	0.030 ±0.005	−0.3	0.88	2.7
4.6	3	−4.61	0.393	3.66	3.01	⋯	⋯	1.2±0.4	2.0±0.6	5.9±2.1	0.010 ±0.002	−0.05	>1.1	>3.9
5.1	5	−5.11	1.60	3.94	−6.23	0.379	12.25	1.7±0.5	2.1±0.7	3.1±1.2	0.0060±0.0016	−0.15	0.83	3.3
5.6	5	−5.56	1.30	4.54	−2.86	− 0.04	6.55	1.6±0.5	2.3±0.9	3.8±1.5	0.0039±0.0011	−0.06	0.80	3.6
6.1	2	−6.32	0.80	5.24	⋯	⋯	⋯	1.4±0.6	1.9±0.6	2.6±1.0	0.0018±0.0007	−0.1	0.74	3.7
6.8	2	−6.53	0.99	4.96	⋯	⋯	⋯	1.5±0.7	2.2±1.2	3.3±1.8	0.0014±0.0007	−0.1	0.78	4.3

Of course, polarization measurements in the pp system at small angles[47–50] show that some helicity-flip amplitudes must be nonzero.

Finally, the near equality of the pp and np diffraction peaks confirm the assumptions of the Regge parametrization of nucleon-nucleon scattering which neglects the ρ and A_2 trajectories. However, the reader must be cautioned that our data are the first measurements of np scattering in this region, that there are systematic uncertainties of the order of 10 or 20%, and that a 10 or 20% effect of the ρ or A_2 trajectory cannot be ruled out.

The values of B are listed in Table II, along with some corresponding values for the pp system. The np values are reasonably consistent with the pp values and the shrinkage of the pp diffraction peak in this region (which is demonstrated by the increasing magnitude of B with energy) appears to be reproduced in the np system. Engler *et al.*[12] very recently measured the neutron-proton diffraction peak for $|t|>0.3$ (GeV/c)^2. Their values of B, of which some are given in Table II, cannot be directly compared with ours because they must use the $|t|$ range $0.3\leq|t|\leq 0.8$ (GeV/c)^2 to evaluate their B parameter, whereas we can use the smaller $|t|$ range $0.1\leq|t|\leq 0.4$ or 0.5 (GeV/c)^2. However, we have made a direct comparison for the incident neutron kinetic energy range of 4–6 GeV and for $0.3\leq|t|\leq 0.8$ (GeV/c)^2. Engler *et al.*[12] find $B=-6.2\pm0.3$ (GeV/c)$^{-2}$, whereas we find $B=-6.08\pm0.22$ (GeV/c)$^{-2}$.

For further examination of the low-momentum region, the reader should refer to the paper of Murray *et al.*[28] on pn quasi-elastic scattering at 991 MeV (1.68 GeV/c incident neutron momentum). In particular, they find the np diffraction peak has $B=-6.91\pm0.25$ (GeV/c)$^{-2}$. The pp system has a smaller value of B [-5.58 ± 0.11 (GeV/c)$^{-2}$] in this region. This is the region where the np total cross section behaves differently from the pp total cross section and where Alexander *et al.*[51] have found some evidence for peculiar behavior in deuteron interactions. Although our results seem to agree with the pp results, this is the region where our experiment is weakest in statistics because the neutron spectrum decreased sharply in this region. Therefore, a new experiment is clearly needed in this region to investigate any np-pp differences.

We next turn our attention to the larger angle region. To obtain a convenient parametrization of the data we have made a weighted least-squares fit for the angular range $|\cos\theta|<0.8$ with the equation

$$\frac{d\sigma}{dt}=\exp\left[\sum_{n=0}^{k} a_n(\cos\theta)^n\right], \qquad (33)$$

where k varied between 2 and 6. This equation allows symmetry effects about $\theta=90°$ to be easily discerned. The value of k for each energy bin was chosen to maximize the χ^2 probability of the fit. In the fit presented, no attempt was made to obtain smooth variations of the parameters a_n with the incident momentum. We did not extend this equation to small angles because in this region the better statistics would force the parameters to fit the diffraction peak. Therefore, this is not an attempt to fit the cross section over the entire angular range, but is primarily a means of smoothing the data in the large-angle region and obtaining a convenient parametrization. Table III presents the parameters for Eq. (33) and the dotted curves in Figs. 11(a) and 11(b) are the fits to this equation. We have not used the data below 3.0 GeV/c because here the measurements end just beyond 90°.

---

[47] P. Bareyre, J. F. Detoeuf, L. W. Smith, R. D. Tripp, and L. Van Rossum, Nuovo Cimento **20**, 1049 (1961).

[48] P. Grannis, J. Arens, F. Betz, O. Chamberlain, B. Dieterle, C. Schultz, G. Shapiro, H. Steiner, L. Van Rossum, and D. Weldon, Phys. Rev. **148**, 1297 (1966).

[49] H. A. Neal and M. J. Longo, Phys. Rev. **161**, 1374 (1967).

[50] G. Cozzika, Y. Ducros, A. de Lesquen, J. Movchet, J. C. Raoul, L. van Rossum, J. Deregel, and J. M. Fontaine, Phys. Rev. **164**, 1672 (1967).

[51] G. Alexander, G. Goldhaber, and B. H. Hall, Lawrence Radiation Laboratory, UCRL Report No. 18365, 1968 (unpublished).

The reader is cautioned against extending the fits beyond the measured regions.

We first consider the question of the symmetry of $(d\sigma/dt)$ about 90°. In order to discuss this more quantitatively it is convenient to define the ratio $F(\theta)=\sigma(\theta)/\sigma(\pi-\theta)$. Values of F for $\cos\theta=0.2$, 0.4, and 0.6 are given in Table III for incident momenta ≥ 4.1 GeV/*c* where the data are extensive enough to permit such a comparison. Another measure of symmetry about 90° is the value of $\theta_{\min}$, the angle at which the cross section attains its minimum. Approximate values of $\cos\theta_{\min}$ are also given in Table III. At 4.6 GeV/*c* and above, $\cos\theta_{\min}$ is statistically in agreement with $\theta_{\min}=90°$. It is clear from the curves in Fig. 11 and the values of $F(\theta)$ and $\cos\theta_{\min}$ that the cross sections become more nearly symmetric in the region $|\cos\theta|<0.4$ at the higher incident momenta.

The significance of this symmetry can be understood from Eq. (17). The symmetry for $|\cos\theta|<0.4$ means that in that region the interference term is small. This can be explained either by the assumption that the phases between the $I=0$ and $I=1$ amplitudes are generally near 90° throughout this angular range, or—what is more likely—that the amplitudes which are antisymmetric about 90° all remain relatively small for $|\cos\theta|\leq 0.4$ at the higher momenta. A similar interference between $I=0$ and $I=1$ amplitudes leads to a deviation of the np polarization from being purely antisymmetric about 90°, so it is likely that the polarization in np scattering will be found small over this angular range. As pointed out before, there must be large interference when $|\cos\theta|$ approaches 1.0. Therefore, either the relative phases of the $I=1$ and the $I=0$ amplitudes change rapidly between $|\cos\theta|=0.4$ and $|\cos\theta|=1.0$, or the antisymmetric amplitudes increase rapidly in this interval.

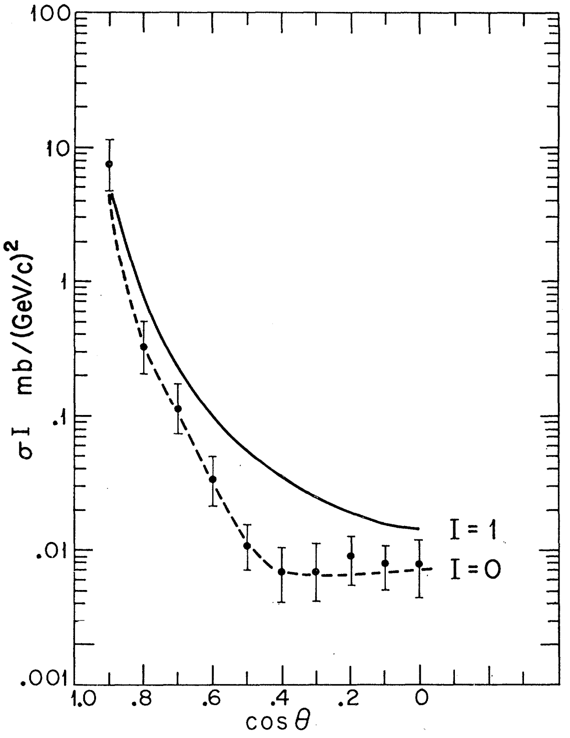

FIG. 14. The elastic differential cross section σ^I at 5 GeV/*c* incident momentum versus the cosine of the c.m. scattering angle. σ^1 is the pp differential cross section $(d\sigma/dt)^{pp}$, and σ^0 is the differential cross section $(d\sigma/dt)^0$ defined in the text.

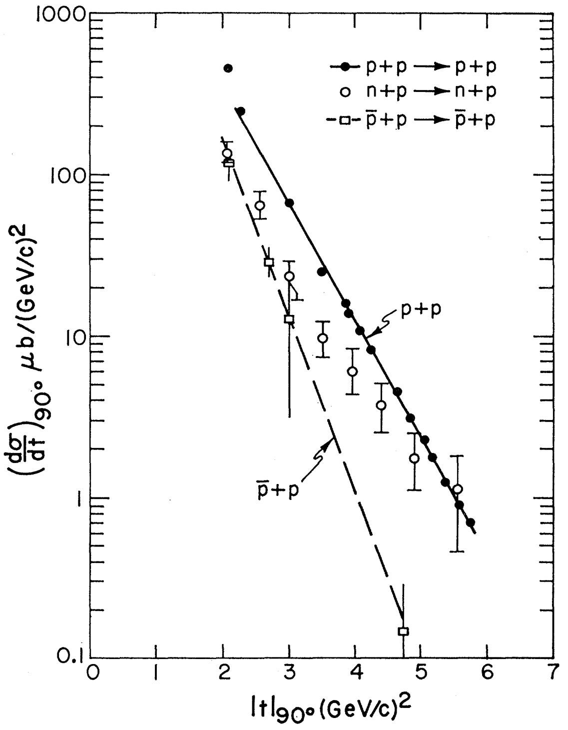

FIG. 13. The differential cross section at 90° for different incident nucleon momenta versus the value of $|t|$ at 90°.

The symmetry as measured by $F(\theta)$ confirms the predictions of Wu and Yang. The theories of Bialas and Czyzewski[18] and of Kastrup[19] must be expanded to take account of the symmetry change at $|\cos\theta|=0.4$.

Another interesting feature of the data is that the cross sections at the higher momenta appear to be nearly independent of θ for a rather large range of θ near 90°. As a measure of this isotropy we list in Table III

TABLE IV. $R=(d\sigma/dt)^{np}(90°)/(d\sigma/dt)^{pp}(90°)$.

Momentum (GeV/*c*)	R
3.0	0.36±0.08
3.6	0.61±0.15
4.1	0.52±0.10
4.6	0.43±0.11
5.1	0.46±0.15
5.6	0.62±0.19
6.1	0.65±0.28
6.8	1.40±0.72

a width $w = |\cos\theta_1 - \cos\theta_2|$, where θ_1 and θ_2 are the two angles at which the fitted cross section reaches twice the value at 90°. The corresponding width in four-momentum transfer, $w_t = |t(\theta_2) - t(\theta_1)|$, is also given. w_t is seen to increase steadily with increasing momentum. No theoretical explanation for this behavior seems to be available. In fact, this observation of the lack of a basic theoretical explanation of the flatness of $(d\sigma/dt)$ near 90° must be extended to the symmetry observation also. The theories we have referred to are very crude, and there is a great need for more basic explanations.

Next we turn our attention to the comparison of *pp* and *np* scattering at 90°. The values of the *pp* and *np* differential cross sections at 90° are plotted against the absolute value of t at 90° for different momenta in Fig. 13. To compare these cross sections we define the ratio $R = (d\sigma/dt)^{np}(90°)/(d\sigma/dt)^{pp}(90°)$. The values of $(d\sigma/dt)^{pp}(90°)$ were obtained from Ref. 43 and from Akerlof *et al.*[52] The values of R are listed in Table IV, and we find the average value of R from 3 to 7 GeV/c is 0.63 ± 0.09. At the highest momenta R rises above 1.0, but the errors are large, and probably the only significant number is the average value of R stated above. The 90° differential cross sections of $\bar{p}p$ are also plotted in Fig. 13.

A recent theory of Krisch[53] on *pp* elastic scattering predicts $R = 0.5$. In addition, the value of R we observe agrees with the second prediction of Wu and Yang, i.e., Eq. (23). These conclusions differ from our previous results[4] because of the changes in the cross-section calculations mentioned above.

Our data seem to disagree with the assumption of no helicity flip [Eq. (15)], since it predicts $R = \frac{1}{4}$. Therefore, the idea that only non-helicity-flip amplitudes are important is only good at small angles and appears to be wrong at large angles.

Since the *pp* and *np* 90° cross sections are similar, we know that the *np* will fit the statistical-model energy dependence prediction of Eq. (20) since the *pp* data do. For the *np* case we find $h = 5.6 \pm 0.7$ GeV^{-1}.

We can find the differential cross section $(d\sigma/dt)^0$, i.e., for the pure $I = 0$ state, using Eq. (8). In Fig. 14 we have plotted $(d\sigma/dt)^0$ and $(d\sigma/dt)^1$ at 5 GeV/c using the *pp* data of Clyde[43] and our *np* data. For $\cos\theta > 0.8$ we have neglected $(d\sigma/dt)^{np}(\pi - \theta)$ because $(d\sigma/dt)^{np}(\pi - \theta)$ is less than $0.1(d\sigma/dt)^{np}(\theta)$. We observe that $(d\sigma/dt)^0$ is about equal to $(d\sigma/dt)^1$ at small angles, but becomes somewhat smaller as 90° is approached.

ACKNOWLEDGMENTS

We are greatly indebted to Fred Martin and to Smith Powell for their contributions to the building, operation, and early analysis of this experiment. Orman Haas, T. L. R. Elder, Ronald Seefred, and James Moss were of great help in the construction and operation of the experiment. Finally, we are grateful to the staff of the Bevatron for their support and help during the setting up and running of the experiment.

---

[52] C. W. Akerlof, R. H. Hieber, A. D. Krisch, K. W. Edwards, L. G. Ratner, and K. Ruddick, Phys. Rev. **159**, 1138 (1967).

[53] A. D. Krisch, Phys. Rev. Letters **19**, 1149 (1967); and private communication.

Fig. 6. A photograph from the experiment with a typical event.